Validation of OpenFOAM with respect to the elementary processes involved in the generation of waves by subaerial landslides

Amir Parvin, Stéphane Abadie, Kamal El Omari, Yves Le Guer

Applied Ocean Research 153 (2024) 104296

Contents lists available at ScienceDirect

Applied Ocean Research

journal homepage: www.elsevier.com/locate/apor

Validation of OpenFOAM with respect to the elementary processes involved in the generation of waves by subaerial landslides

Amir H. Parvin [a], Stéphane Abadie [a,*], Kamal El Omari [b], Yves Le Guer [c]

[a] Université de Pau et des Pays de l'Adour, E2S UPPA, SIAME, Anglet, 64600, France
[b] Université de La Réunion, Laboratoire Piment, Saint Pierre, 97455, France
[c] Université de Pau et des Pays de l'Adour, E2S UPPA, SIAME, Pau, 64000, France

ARTICLE INFO

Keywords:
Tsunami
Landslide
Energy
Wave breaking
OpenFOAM

ABSTRACT

This study presents a validation of the OpenFOAM multiphase solver (i.e., `multiphaseInterFoam`) with respect to the elementary processes involved in the simulation of waves generated by high mobility subaerial landslide with a specific focus on the computation of energy terms. These processes include slide flow over a slope, impulse wave generation, wave dispersion, wave propagation and breaking. The simulations are conducted in 2D. The results allow to determine the minimum number of cells and the appropriate model tuning to reach acceptable accuracy while maintaining the computation time in a reasonable limit. To respect energy conservation, the choice of the turbulence model appears critical. Only, with a turbulence including a buoyancy term in the equations to account for the multiphase flow, and optimized initial values of the turbulence model parameters, could be the energy components of the flow accurately calculated. This study highlights the complexity of the phenomenon and the care with which, simulations should be conducted for the accurate computation of the energy transfers in the context of subaerial landslides.

1. Introduction

The simulation of impulse waves generated by subaerial landslides poses great challenges to the scientific community as it involves complex slide rheology, turbulent flows and free surface processes. To address this complexity, advanced models are developed and need to be properly validated. It is the objective of the present study to provide a thorough validation of one of the most used model in the community (i.e., OpenFOAM) including original aspects which will be developed further.

Landslide wave models are usually composed of a slide model coupled with a hydrodynamic model. For subaerial landslides, the hydrodynamic model should be able to describe the full range of physical processes occurring, such as vertical flow acceleration, vortices and multiple interface reconnections due to wave breaking for instance. This disqualifies models based on strong physical assumptions such as shallow water models (Cecioni and Bellotti, 2010) or more generally depth-integrated models (Tarwidi et al., 2022), boundary elements models (Grilli et al., 2002), non-hydrostatic Navier–Stokes models assuming a single valued water surface (Ma et al., 2015). Note that if these models cannot represent the whole complexity of the generation area, they may be able to obtain satisfactory results in the far field.

Navier–Stokes models with a VOF algorithm for the interfaces treatment are the most common alternative to simulate the phenomenon. Here, we restrict our review to works focused on subaerial landslides impulse waves. The modeling community needs reference cases to which models can be compared, for validation purpose. At first, the experimental works presented in Fritz (2001), Fritz et al. (2003), involving 2D granular subaerial slides with high impact velocities, were extensively used to validate subaerial landslide impulse wave models. Hence, Weiss et al. (2009) compared the results obtained with the multi-material hydrocode iSALE (Impact Simplified Arbitrary Lagrangian Eulerian) with Fritz (2001). Basu et al. (2010) employed the FLOW3D solver with three phases and two different turbulence models to simulate the same reference case. A comparable work was made in Biscarini (2010) using the FLUENT solver. Abadie et al. (2010) also qualitatively compared the results obtained using THETIS, a Navier–Stokes VOF model with three Newtonian phases, run in laminar flow condition, with the experimental snapshots of a subaerial granular slide penetrating water (Fritz et al., 2003). The first 2D experiments of Fritz (2001), Fritz et al. (2003) were later completed by 3D measurements in Mohammed and Fritz (2012). These experiments were, for instance, used as validation case in Kim et al. (2020) for the

* Corresponding author.
E-mail addresses: aparvinashti@univ-pau.fr (A.H. Parvin), stephane.abadie@univ-pau.fr (S. Abadie), kamal.el-omari@univ-reunion.fr (K.E. Omari), yves.leguer@univ-pau.fr (Y.L. Guer).

https://doi.org/10.1016/j.apor.2024.104296
Received 18 June 2024; Received in revised form 26 September 2024; Accepted 26 October 2024
Available online 7 November 2024

TSUNAMI3D model. Viroulet et al. (2013) conducted an experimental study involving, among others, a triangular granular subaerial slide released from a resting position located just above the water free surface. Abadie et al. (2020) and Paris et al. (2021) simulated this experiment respectively with THETIS and the multiphase solver of OpenFOAM (i.e., the `multiphaseInterFoam`), considering a Newtonian slide with a calibrated viscosity. Similarly, Battershill et al. (2021) simulated the experiment described in Bougouin et al. (2020-05) involving a granular pyroclastic density current with the model Basilisk also considering a Newtonian flow. Romano et al. (2023) used a Coulomb viscoplastic rheology implemented in the standard solver `multiphaseInterFoam` to simulate the experiments of Viroulet et al. (2013) and Mohammed and Fritz (2012) without the need of any parameter calibration.

All the previous studies considered the slide as a continuous phase, either Newtonian or non Newtonian, but with no possibility for the water flow to penetrate within the granular phase, whereas this obviously occurs in the natural phenomenon as well as in most of the experiments. Notable efforts have been made to overcome this limitation in the recent years. A two phase model for the granular mixture coupled with a VOF approach for the other fluid phases has been employed successfully for instance in Si et al. (2018) and in Rauter et al. (2022). The coupling of DEM (Discrete Element Method), for the slide phase, and other approaches, for water and air phases, appears in this respect, also as an interesting alternative. The DEM method can be, for instance, coupled with mesh-based algorithms as in Mao et al. (2020) and Bilal et al. (2021). Other authors choose to employ a complete Lagrangian strategy by coupling the DEM method with the SPH particle-based method (Tan and Chen, 2017; Xu et al., 2020; Zhou et al., 2022). Other possible research strategies include the two-phase material point method as in Zhao et al. (2022, 2023) which is one of the latest developments in particle-in-cell (PIC) methods (Harlow, 1964). Note that this type of methods can also be coupled with the DEM approach as in Chen et al. (2019).

The validations proposed in these papers are based on the parameters measured in the experimental studies. They include the velocity and thickness of the slide at the moment of impact (Clous, 2018), the final position and shape of the landslide (Wang et al., 2017), snapshots of slide-water impact completed with the velocity field in the case of available PIV measurements (Basu et al., 2010; Abadie et al., 2010), free surface time signal obtained with wave gauges (most of the studies) and wave run-up over the shore ending the domain Kim et al. (2020).

From the previous literature review, it appears that most of the studies focused on the granular slide interaction with water, which indeed involves physical processes challenging the current numerical models. A notable exception is the experimental work described in Bullard et al. (2019) which featured a water slide, a limit case representative of the highest landslide mobility. Nevertheless, the obvious advantage of such case is that it can be reproduced by classical numerical models relatively easily without any need for artificial calibration. The measurements of Bullard et al. (2019) were later simulated in Rauter et al. (2021) with `multiphaseInterFoam`. The model showed difficulties in reproducing the water slide shape while the slide velocity and the wave field were correctly simulated.

Most of the numerical studies also focused on the maximum wave amplitude observed in the near field. It has the advantage to reduce the computational domain to the generation zone and therefore limits the computational cost to reasonable bound. Nevertheless, after reaching this maximum amplitude, the impulse wave is frequently breaking. Battershill et al. (2021) report a wide range of wave breaking behaviors which, each, should lead to different energy dissipation rates. Fritz et al. (2004) observed several types of waves in their experiment involving: weakly nonlinear oscillatory waves, nonlinear transition waves, solitary-like waves and dissipative transient bores. Breaking was reported for the majority of the cases tested. Wave dispersion effect on the leading wave was also clearly observed.

The impulse wave transformation after generation is rarely addressed in the numerical studies. This implies a very long computational domain and a validation of the model with respect to complex processes including breaking. Rauter et al. (2021) compared the wave simulated at different gauge positions including the post breaking area with the measurements of Bullard et al. (2019). The results obtained with `multiphaseInterFoam` appeared quite satisfactory regarding the wave amplitude decay.

In particular, the leading wave energy evolution with time seems crucial to properly simulate for a relevant hazard assessment. Energy transfers have been already studied numerically in Clous and Abadie (2019) or Battershill et al. (2021), for instance. Nevertheless, to the best knowledge of the authors, the energetic aspect is never considered at the validation stage.

The numerical simulation of such a complex phenomenon requires the use of a multi-purpose calculation code which integrates models to account for the three-phase nature of the flow, the non-Newtonian rheology of the slide and turbulence. Furthermore, it must allow the testing of different models, possess a degree of flexibility with regard to the mesh and the capacity to perform sufficiently advanced post-processing for the calculation of energy exchanges. For these reasons, we opted for OpenFOAM and more specifically its multiphase solvers: `interFoam` and `multiphaseInterFoam`.

In this article, we present a thorough validation of these two solvers in 2D, with respect to the physical processes involved in subaerial landslide wave generation and transformation, accounting for the energetic aspects. In the path of Bullard et al. (2019) and Rauter et al. (2021), the slide is simplified compared to the usual granular rheology and only Newtonian and non-Newtonian slides are considered. The processes considered are: slide propagation, impulse wave generation, propagation, dispersion and breaking. They should be, each, properly resolved by the model to ensure the simulation accuracy as they act sequentially, and therefore, influence the final result (i.e. the amount of energy transported by the wave). Consequently, and conversely to previous works presented in this introduction, the approach chosen in the paper, is to propose a validation for each process, considered individually. The other original aspect of this study is the consideration of the energy conservation and dissipation calculation in the validation process. The final objective is to provide useful recommendations, essentially in terms of minimum mesh resolution and model choices, to ensure the liability of the results for future studies, including energy transfer assessments.

The paper is structured as follows. Section 2 presents the numerical model and the computation of the energy components. The turbulence models tested in this work are presented in detail, as this aspect is of key importance with regard to the energy transfers. Section 3 presents the validation cases studied and the results obtained for the following flow configurations:

- non-Newtonian slide flowing over a slope,
- impulse wave generation and breaking,
- wave dispersion (case of the undular bore),
- energy conservation in a propagating solitary wave,
- energy conservation in a breaking solitary wave,
- dissipation computation in a turbulent bore.

Finally, Section 4 discusses the different results obtained and Section 5 gives the conclusions of the work.

2. Methods

2.1. Numerical method

In this work, depending on the problem case (i.e., water and air, slide and air, or slide, water and air), the two-phase (`interFoam`) or the multi-phase (`multiphaseInterFoam`) OpenFOAM VOF solver is

used. These models solve the Navier–Stokes equations for multiphase flow of incompressible immiscible fluids.

The phase-fraction for phase i is first defined as follows:

$$\alpha_i(x,t) = \begin{cases} 1 & \text{if phase } i \text{ is present at } x,t \\ 0 & else. \end{cases} \tag{1}$$

The continuity and momentum equations respectively read:

$$\nabla \cdot \mathbf{u} = 0 \tag{2}$$

$$\frac{\partial \rho \mathbf{u}}{\partial t} + \nabla \cdot (\rho \mathbf{u}\mathbf{u}) = -\nabla p + \nabla \cdot (2(\mu + \mu_t)\mathbf{D}) + \rho \mathbf{g} + f_{\sigma i}, \tag{3}$$

with $\mathbf{u}$ the fluid local velocity, $\mathbf{g}$ the gravitational acceleration, $p(x,t)$ the pressure field, $\rho(x,t)$, $\mu(x,t)$ and μ_t the local fluid density, molecular dynamic viscosity and turbulent (eddy) viscosity (see Section 2.2), respectively. $\mathbf{D} = \frac{1}{2}(\nabla \mathbf{u} + (\nabla \mathbf{u})^T)$ is the strain rate tensor, while $f_{\sigma i} = \sigma \kappa \nabla \alpha_i$ is the surface tension force, modeled as a continuum surface force (Brackbill et al., 1992), in which σ is the surface tension at the interface and κ the local curvature of the interface.

The local fluid properties are averaged among the existing phases in a computational cell following:

$$\rho(x,t) = \sum_{i=1}^{N} \alpha_i(x,t)\ \rho_i, \qquad \mu(x,t) = \sum_{i=1}^{N} \alpha_i(x,t)\ \mu_i, \tag{4}$$

with N number of phases and ρ_i and μ_i density and molecular dynamic viscosity of an existing phase in a cell.

The phase fraction value is updated at each time step thanks to the phase fraction advection equation given by:

$$\frac{\partial \alpha_i}{\partial t} + \nabla.(\alpha_i \mathbf{u}) + \sum_{j}^{adjacent\ cells} \nabla \cdot (\alpha_i \alpha_j u_{r,ij}) = 0. \tag{5}$$

Here $u_{r,ij}$ is the relative velocity between phases. The last term is employed as a numerical technique to ensure a sharp and non-diffusive interface.

The time and space computational domains are discretized into a finite number of time steps and cells to solve the governing equations. Spatial discretization is the standard Gaussian finite-volume integration method based on summing values on cell faces, which must be interpolated from cell centers (Greenshields, 2018).

Eqs. (2) and (3) are solved with the PIMPLE algorithm which takes care of the pressure–velocity coupling.

The CFL condition ensures the stability of the solution by limiting the time step Δt following:

$$CFL = \frac{|\mathbf{u}|\ \Delta t}{\Delta x} < 1, \tag{6}$$

The phase volume fractions equation (5) is solved with the MULES (Multidimensional Universal Limited Explicit Solver) algorithm to ensure the conservation of sharp interfaces between a pair of phases.

2.2. Turbulence models

2.2.1. Reynolds averaged Navier–Stokes equations

As formerly mentioned, energy processes is an important aspect of this work. Therefore, turbulence should be properly resolved as it plays a critical role in the energy distribution in the flow as well as in the dissipation processes. The following section describes the different turbulent models which have been tested.

In the Reynolds averaged Navier–Stokes (RANS) equations, the flow variables are decomposed in averaged and fluctuating components. Eqs. (2) and (3) involve averaged flow components (velocity and pressure). When deriving the RANS equations, a new tensor made up of fluctuating velocities products appears in the equations, which under the Boussinesq hypothesis (Boussinesq, 1877), can be expressed in function of a turbulent viscosity μ_t as written in Eq. (3). The turbulent kinetic energy (TKE) of the flow is given by $k = \frac{1}{2}\overline{\mathbf{u}' \cdot \mathbf{u}'}$ with $\mathbf{u}'$ the fluctuating velocity and the $\overline{()}$ symbol, the time averaging operator. The rate of dissipation of the turbulent kinetic energy per unit mass is $\epsilon = \frac{1}{2}\frac{\mu}{\rho}\overline{\left[\nabla \mathbf{u}' + (\nabla \mathbf{u}')^T\right]} : \left[\nabla \mathbf{u}' + (\nabla \mathbf{u}')^T\right]$. The different models detailed hereafter differs on their expression of the three variables μ_t, k and ϵ.

2.2.2. Standard k-ϵ model

In this model, the eddy viscosity is $\mu_t = \rho\ C_\mu \frac{k^2}{\epsilon}$. The governing equations for k and ϵ are:

$$\frac{\partial \rho\, k}{\partial t} + \nabla \cdot (\rho\, k\, \mathbf{u}) = \nabla \cdot \left(\left(\frac{\mu_t}{\sigma_k} + \mu\right) \nabla k\right) + P_k - \rho\epsilon, \tag{7}$$

$$\frac{\partial \rho\, \epsilon}{\partial t} + \nabla \cdot (\rho\, \epsilon\, \mathbf{u}) = \nabla \cdot \left(\left(\frac{\mu_t}{\sigma_\epsilon} + \mu\right) \nabla \epsilon\right) + \frac{C_{1\epsilon}\, \epsilon}{k} P_k - \frac{\rho\, C_{2\epsilon}\, \epsilon^2}{k}, \tag{8}$$

where $P_k = 2\mu_t D_{ij} D_{ij}$ is the production of turbulent energy. Recommended values for the constants of the model C_μ, σ_k, σ_ϵ, $C_{2\epsilon}$ are 0.09, 1.0, 1.3, 1.44, 1.92, respectively (Rodi, 1980). In the derivation of the standard k-ϵ model, the flow is assumed to be fully turbulent and the effects of molecular viscosity, negligible. Therefore, in theory, it cannot be integrated all the way to the wall (Moukalled et al., 2016).

2.2.3. RNG k-ϵ model

The renormalized group (RNG) k-ϵ model was developed in order to improve the behavior of the standard k-ϵ model in the case of high streamline curvature flows such as, flows over a backward-facing step for instance. It consists basically on a modification of a coefficient in the ϵ equation, to account for the interaction between the turbulent dissipation and the mean shear (Yakhot et al., 1992).

In the RNG k-ϵ model, the k and ϵ equations are similar to Eqs. (7) and (8). The only change is on the coefficient $C_{1\epsilon}$ replaced by:

$$C^*_{1\epsilon} = C_{1\epsilon} - \frac{\eta\,(1 - \eta/\eta_0)}{1 + \beta\eta^3}. \tag{9}$$

In (9), η is the additional expansion parameter used in the derivation by Yakhot et al. (1992), defined as the time scale ratio of the turbulent to the mean strain rate, ($\eta = \dot{\gamma}\, k/\epsilon$).

C_μ, σ_k, σ_ϵ, $C_{\epsilon 1}$, $C_{\epsilon 2}$, η_0 and β are equal to 0.0845, 0.71942, 0.71942, 1.42, 1.68, 4.38 and 0.012, respectively (Openfoam-code, 2023).

2.2.4. Nonlinear k-ϵ model

The nonlinear k-ϵ model (NL) is a wall-bounded model proposed by Shih (1993) and Shih et al. (1996). Unlike the standard k–ϵ model, this model does not produce negative normal stresses in particular situations of complex turbulent flows. The NL model connects the mean strain rate of the flow to the Reynolds stress tensor using the quadratic algebraic nonlinear Reynolds stress model. In this model, the Reynolds stress tensor reads:

$$\boldsymbol{\tau}^{\boldsymbol{R}}_{\boldsymbol{nl}} = \frac{2}{3}\rho\, k\, \mathbf{I} - \mu_t\, 2\mathbf{D} + \boldsymbol{\tau}_{\boldsymbol{nl}} \tag{10}$$

with the following expression for the additional nonlinear stress term:

$$\boldsymbol{\tau}_{\boldsymbol{nl}} = \frac{1}{2}(\chi + \chi^T) \tag{11}$$

where:

$$\chi = \frac{k^3}{(A_2 + \eta^3)\,\epsilon^2}\ \Big(C_{\tau 1}\left[\nabla \mathbf{u} \cdot \nabla \mathbf{u} + (\nabla \mathbf{u} \cdot \nabla \mathbf{u})^T\right] + C_{\tau 2}\left[\nabla \mathbf{u} \cdot (\nabla \mathbf{u})^T\right] + C_{\tau 3}\left[(\nabla \mathbf{u})^T \cdot \nabla \mathbf{u}\right]\Big). \tag{12}$$

The definition of the parameter η is the same as in the RNG k-ϵ model. k and ϵ equations are identical to the RNG k-ϵ model. The eddy viscosity is obtained through the general relationship of the standard k-ϵ model, except that the value of C_μ depends upon the values of ξ and η by:

$$C_\mu = \frac{2}{3\,(A_1 + \eta + \alpha_\xi\, \xi)}, \tag{13}$$

where α_ξ and A_1 are constants and $\xi = \Omega\frac{k}{\epsilon}$ is an additional scalar parameter defined in terms of the mean rate of rotation, $\Omega = \sqrt{2\,\boldsymbol{\Omega} : \boldsymbol{\Omega}}$, with the rotation tensor $\boldsymbol{\Omega}$ equal to $\frac{1}{2}(\nabla\mathbf{u} - (\nabla\mathbf{u})^T)$. Default values for the constants used in the nonlinear k-ϵ model are 1.44, 1.92, 1, 1.3, 3, 15, −19, 1.25, 0.9 and 1000 for $C^*_{\epsilon 1}$, $C^*_{\epsilon 2}$, σ_ϵ, σ_k, $C_{\tau 1}$, $C_{\tau 2}$, $C_{\tau 3}$, A_1, α_ξ and A_2, respectively.

2.2.5. k-ω and k-ω SST models

The k-ω turbulence model was originally developed by Wilcox (1988) to address the limitations of k-ϵ family models in resolving flows with adverse pressure gradients and near-wall flows. A new variable is introduced, ω, which is the specific rate of turbulent dissipation, namely the rate at which turbulent kinetic energy is dissipated. This type of model also solves two transport equations to predict the turbulent flow properties.

The k-ω Shear-Stress Transport (SST) model introduced first by Menter (1994) is a variant of the k-ω model. It is an extension of the standard k-ω model which combines elements of both k-ω and $k-\epsilon$ models by using blending factors. This way, the k-ω SST model tends to the k-ω model in the near-wall region and to the $k-\epsilon$ model away from the wall. This makes it versatile and suitable for a wider range of flows, including both wall-bounded and free-stream flows. The current build-in k-ω SST models of OpenFOAM use the formulation of Menter et al. (2003). The governing equations read:

$$\frac{\partial \rho\, k}{\partial t} + \nabla\cdot(\rho\, k\, \mathbf{u}) = \nabla\cdot\left(\left(\mu + \sigma_k\, \mu_t\right)\, \nabla k\right) + P_k - \rho\, \beta^*\omega k, \tag{14}$$

$$\frac{\partial \rho\, \omega}{\partial t} + \nabla\cdot(\rho\, \omega\, \mathbf{u}) = \nabla\cdot\left(\left(\mu + \sigma_\omega\, \mu_t\right)\, \nabla\omega\right) + \frac{\gamma}{\nu_t}\cdot G - \rho\beta\omega^2 + 2\rho(1-F_1)\cdot\frac{\sigma_{\omega 2}}{\omega}\cdot\nabla k\cdot\nabla\omega. \tag{15}$$

where:

$$G = \rho\nu_t|\dot{\gamma}|^2, \qquad P_k = min(G, 10\rho\beta^*\, k\omega), \qquad \nu_t = \frac{a_1 k}{max(a_1\,\omega, \sqrt{2}\,\dot{\gamma}\,F_2)}, \tag{16}$$

$$\phi = F_1\phi_1 + (1-F_1)\phi_2, \tag{17}$$

β^* and a_1 values are 0.09 and 0.31, respectively. F_1 and F_2 are blending functions. F_1 is equal to 1 in the near wall region (activating k-ω) and 0 away from the nearest wall (activating k-ϵ). Coefficients σ_k, σ_ω, β and γ are calculated through the generic equation (17). Hence, each constant is a blend of an inner constant (subscript 1) and an outer constant (subscript 2) (Brown et al., 2016).

2.2.6. Modified turbulent models for multi-phases simulations

Turbulence models in their original form do not take into account the density or viscosity gradient present around the air–water interface. Implemented in a classical VOF model, they produce excessive turbulent kinetic energy near the interface due to this gradient. Some authors addressed this issue by introducing a buoyancy term G_b in the TKE equation, suppressing this artificial turbulence near the water surface (Devolder et al., 2017), as:

$$G_b = -\frac{\nu_t}{\sigma_t}\cdot\nabla\cdot\rho\,\mathbf{g} \tag{18}$$

The constant scalar $\sigma_t = 0.85$ determines how much buoyancy is introduced. This method switches to a laminar regime near the surface, preventing excessive surface wave damping, while restoring the original model in zones with a horizontal density gradient (as $G_b = 0$ in this case). In addition to the buoyancy term, Larsen and Fuhrman (2018) also implemented a limiter factor in order to decay the non-physical TKE dissipation rate that occurs in the simulation due to the presence of an identified instability in the turbulence model.

2.3. Herschel–Bulkley viscoplastic model

In this work, we considered a viscoplastic slide governed by the Herschel–Bulkley law. The latter is a generalization of the Bingham plastic model to include the nonlinear behavior of the flow when the yield stress (τ_0) is exceeded. In a one-dimensional steady shearing motion, the Herschel–Bulkley constitutive law is written as:

$$\begin{aligned} \tau_{yx} &= \tau_0 + K(\dot{\gamma_{yx}})^n \quad \text{for } |\tau_{yx}| > |\tau_0| \\ \dot{\gamma_{yx}} &= 0 \quad\qquad\qquad\ \text{for } |\tau_{yx}| < |\tau_0|, \end{aligned} \tag{19}$$

where K and n are the consistency index and power-law index parameters, respectively (Chhabra and Richardson, 1999). Note that the dimensions of K depend upon the value of n.

Modeling an actual discontinuous rheological behavior (i.e., a solid behavior when the shear stress is below the yield stress and a fluid behavior otherwise) is difficult. Usually, a regularized model is applied to overcome this issue (Beverly and Tanner, 1992). For low strain rates, the material is modeled as a highly viscous fluid with viscosity ν_0. Beyond a threshold, the kinematic viscosity follows the intended rheological law in correspondence with the strain rate value (Greenshields, 2018). For the Herschel–Bulkley model, the apparent viscosity is given by the following relation:

$$\nu = min\,(\nu_0,\ \frac{\tau_0}{\dot{\gamma}} + K\,\dot{\gamma}^{n-1}), \tag{20}$$

Eq. (20) is the law used in OpenFOAM and in the present work.

2.4. Computation of energy and dissipation in each phases at time t

At each time step, the mechanical energy E_m of each phase m is the sum of the potential and kinetic energy. Both terms can be calculated thanks to the simulation variables.

The global kinetic energy of phase m is the sum of the mean flow kinetic energy and the turbulent kinetic energy within this phase. It is therefore obtained through the following relation:

$$E_{k,m}(t) = \iint_A \alpha_m(t)\ (\frac{1}{2}\ |\mathbf{u}(\mathbf{t})|^2\ + k(t)\ )\ \rho_m\ dx\,dy \tag{21}$$

The two kinetic components should be accounted for as there are continual exchanges between the mean and the turbulent flows. Without k, the global energy balance would not be complete. In Eq. (21), A denotes the computational area.

The potential energy of phase m is:

$$E_{p,m}(t) = \iint_A \alpha_m(t)\ g\ y(t)\ \rho_m\ dx\,dy \tag{22}$$

with y, the vertical coordinates of the point in a given reference system. Here, the reference is at the water surface at rest.

Note that, in the particular case of water, the potential energy of the wave field is obtained by removing the initial water potential energy as:

$$E_{p,wave}(t) = \iint_x \alpha_w(t)\ \rho_w\ g\ y(t)\ dx\,dy - \int_0^{h_0}\int_x \rho_w\ g\ y(t)\ dx\,dy, \tag{23}$$

where h_0 is the initial water depth. For the cases of waves generated by a landslide, the integration in the horizontal direction starts from the slide tip as described in Clous and Abadie (2019).

Physical dissipation is acting in each phase to dissipate the energy into heat. The amount of energy dissipated at time t_1 is the integration in time of the energy dissipation rate $\boldsymbol{\Phi}(t)$. Hence:

$$\begin{aligned} E_{diss,m}(t_1) &= \int_0^{t_1} \boldsymbol{\Phi}(t)dt \\ &= \int_0^{t_1}\iint_A (\alpha_m(t)\ \mu_m\ \dot{\gamma}(t)\dot{\gamma}(t)\,dx\,dy + \alpha_m(t)\ \epsilon(t)\ \rho_m\,dx\,dy)\,dt, \end{aligned} \tag{24}$$

where $\dot{\gamma}(t)$ denotes the scalar shear rate value in the cell. This dissipation is the sum of two components. The first one is the dissipation

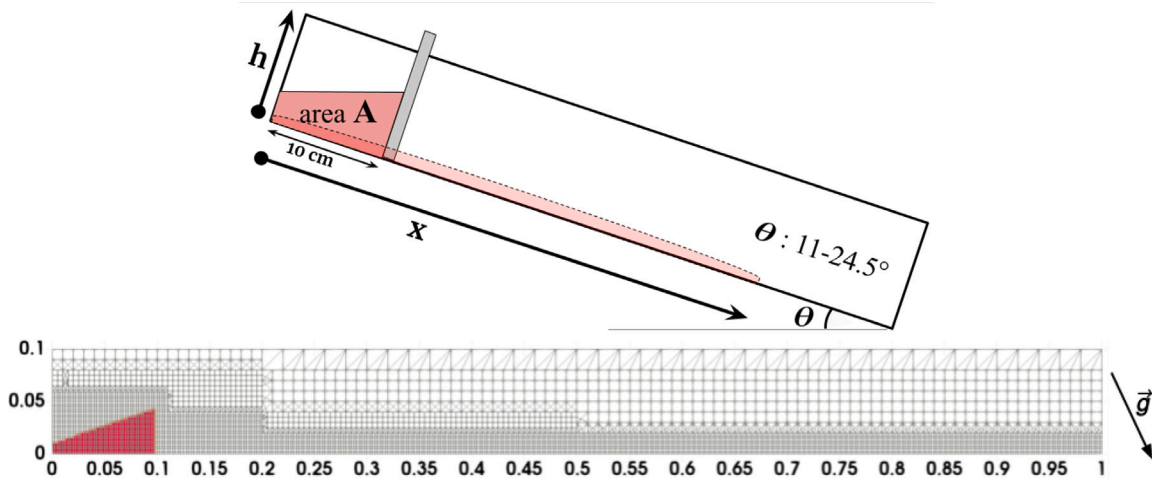

Fig. 1. Top Panel: Schematic view of the experimental setup simulated. Bottom Panel: Example of mesh corresponding to the simulation of case (a) in Huang and García (1998). In this example, the finest mesh cell is 2.5 mm. The initial slide phase is also provided in red (left part of the domain).

at the molecular scale, the second one, the dissipation of turbulence into heat. For a global energy balance, both contributions should be accounted for.

At each time step, the total energy E_T in the system including all the phases, can be computed as:

$$E_T(t) = \sum_{m=1}^{N} E_m(t) \tag{25}$$

with N the number of phases.

Theoretically, in a closed system, E_T should only decrease with time and the decrease should corresponds perfectly to the amount of physical dissipation over the duration considered. Therefore, we may write:

$$-\left(E_T(t_2) - E_T(t_1)\right) = \int_{t_1}^{t_2} \Phi(t)dt \qquad (t_2 > t_1) \tag{26}$$

Nevertheless, inherently, due to discretization approximations (numerical dissipation) or inconsistencies in the turbulence model, globally speaking, there is always some differences between the two quantities. Therefore, Eq. (26) should be rewritten as:

$$-\Delta E_T(t_1,t_2) = -\left(E_T(t_2) - E_T(t_1)\right) = \int_{t_1}^{t_2} \Phi(t)dt + \Delta E_{error}(t_1,t_2) \tag{27}$$

And finally, the energy conservation error of the model between times t_1 and t_2 can be expressed as:

$$\Delta E_{error}(t_1,t_2) = -\Delta E_T(t_1,t_2) - \int_{t_1}^{t_2} \Phi(t)dt \tag{28}$$

The problem of energy conservation is rarely, if not never, addressed in most papers based on CFD simulations. It is however a critical point when studying energy exchanges as in the present work.

3. Validation cases and results

Table 1 provides an overview of the various validation cases studied in this paper and presents the different model configurations employed for each. The mesh features are indicated in column 3 and 4. The cell size is uniform for all the cases (resolution, which may vary depending on the simulation, indicated in column 3), except for cases (1), (2) and (5), for which a special cell arrangement was required. For these cases, a representation of the mesh is provided. Additionally, for all the cases, the kinematic viscosity and density of water and air are 10^{-6} ($m^2\ s^{-1}$), 1000 ($kg\ m^{-3}$), 1.48×10^{-5} ($m^2\ s^{-1}$) and 1 ($kg\ m^{-3}$), respectively. The scheme used to discretize the convective terms of Eqs. (3) is the most important factor controlling the value of the numerical dissipation (Eq. (28)). In OpenFOAM, there are various schemes available, like the classical Upwind or QUICK schemes for instance, each having strong and weak points. Hence, Upwind is unconditionally stable but far too diffusive. Whereas QUICK is accurate but tends to create artificial oscillations. Among these, during the numerous tests conducted in this study, the second order accurate Linear Upwind scheme appeared to be a good compromise between accuracy and stability. Therefore, it is the scheme finally used in the simulations presented hereafter.

3.1. CASE 1: Slide flow — validation of the non-Newtonian rheological model

This section presents a validation case based on the experimental and analytical results of Huang and García (1998). The setup consisted of an adjustable tilted Plexiglas tank 100 cm long and 30 cm wide. In the upstream section, a 10 cm long reservoir, with an area of A, released a kaolin–water mixture with varying volumetric concentrations ($C_v = V_{solid}/(V_{solid} + V_{water})$) over a slope of an angle θ through a sliding gate. Table 2 provides the parameters of the three experiments conducted.

The objective is here to validate the Herschel–Bulkley rheology model implemented in OpenFOAM in a configuration close to a slide flow. Fig. 1 shows an example of a mesh used for case (a). The domain is split in different zones, each featuring an adapted resolution. In particular, in the zone in which the fluid moves, the cell size is the finest. Indeed, the shear rate generated in the boundary layer adjacent to the bottom plays a key role in determining the non-Newtonian fluid viscosity and should be properly resolved. Moreover, the experimental results show that the slide thickness drops very quickly to very small values (< 1 cm), therefore, the mesh had to adapt to this feature.

In the example presented in Fig. 1, the cell size in this zone is 1.25 mm. Note that in the computational domain, the gravity vector is tilted to reproduce the effect of the slope angle. In the present study, we tested different meshes, with the following (finest) cell sizes: 0.625 mm, 0.833 mm, 1.25 mm, and 2.5 mm, to conduct a sensitivity study.

Figs. 2 and 3 show a comparison between the simulations for different meshes, the experimental data and the analytical solution presented in Huang and García (1998). The first figure (Fig. 2) shows the snapshots of the mixture air interface. Since the time corresponding to these snapshots is not provided in Huang and García (1998), simulated snapshots are taken when the computed front are the closest to the corresponding measurements. The front evolution with time is compared in the next figure. Huang and García (1998) shows that the average slide thickness is well predicted by the model. On case (a), with the lowest resolution, the accuracy of the numerical simulation

Table 1
Model setup for each validation case considered in this study. The work of the following references was used for the comparisons: Huang and García (1998), Jánosi et al. (2004), Soares Frazao and Zech (2002), Wroniszewski et al. (2014), Li and Raichlen (2003), Yeh et al. (1989) and Mauriet (2009).

General purpose	(#) Case	Cell dimension (mm) $\Delta x \times \Delta y$	# cells within reference parameter[a]	Bottom BC	Solver	Turbulence	CFL
slide flow	(1) Rheology	2.5 × 2.5 1.25 × 1.25 0.83 × 0.83 0.625 × 0.625	4–12	no-slip	`interFoam`	laminar	0.5
wave generation and breaking	(2) Jánosi moving gate	5 × 5 (2 × 2)[b]	12	No BC	`overInterDyMFoam`	$k-\omega$ SST (Devolder et al., 2017)	1
	(2) Jánosi 2-3phases	5 × 5	12	no-slip	`interFoam` `multiphaseInterFoam`	$k-\omega$ SST (Devolder et al., 2017)	0.1
wave dispersion	(3) Undular bore	20 × 2 20 × 5 40 × 5 100 × 5	7–15	no-slip	`interFoam`	$k-\omega$ SST (Devolder et al., 2017)	0.1
energy processes	(4) Propagating solitary	68.8 × 68.8 34.4 × 34.4 17.2 × 17.2	4–15	free-slip	`interFoam`	laminar	0.2
	(5) Breaking solitary	5 × varies 2.5 × varies	40–80	no-slip	`interFoam`	varies (Table 5)	0.5
	(6) Turbulent bore	10 × 10 5 × 5 2 × 2	10–40	free-slip	`interFoam`	$k-\omega$ SST (Devolder et al. (2017))	0.1

[a] The "reference parameter" is different in each case. For the slide case, it is the slide thickness, it is wave height for the propagating wave, and the breaking wave height at the moment of breaking for all the cases involving a breaking wave.
[b] Represents the dynamic mesh zone resolution.

Table 2
Rheological parameters (equation (20)) measured for the different kaolin–water suspensions used in the three experiments of Huang and García (1998).

Cases –	C_v %	Bulk density, ρ (gr cm^{-3})	τ_0 (N m^{-2})	K (N m^{-2} s^n)	n –	A (cm^2)	θ degree
a	21.07	1.348	14.10	10.20	0.34	29.2	18.5
b	19.59	1.323	9.96	7.10	0.38	32.4	24.5
c	13.05	1.215	2.21	0.22	0.75	24.7	11

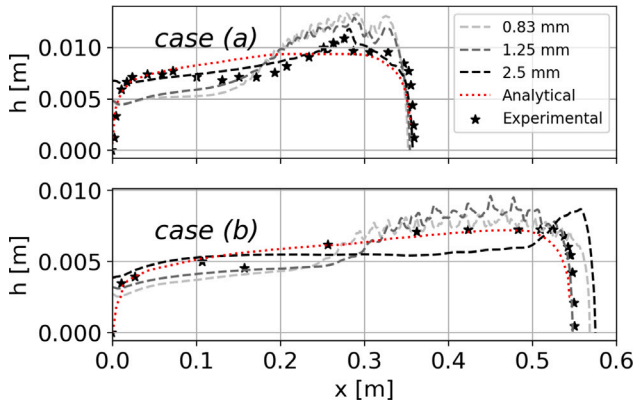

Fig. 2. Snapshots of the simulated kaolin-water mixture free surface for different meshes in cases (a) and (b), (see Table 2) and comparison with the experimental and analytical results of Huang and García (1998).

is very satisfactory. Nevertheless, as the resolution increases, larger discrepancies with the measured reference are observed. In particular, a few oscillations are visible in the slide shape simulated in a zone where a strong shear flow is expected and the slide thickness in this area is also exaggerated. For the lower viscosity of case (b), this behavior is less pronounced but the oscillations remain. Fig. 3 shows the slide front displacement and the hydrograph for the less dense and viscous case (i.e., case (c)). Physically, in the initial stages of motion, the slide encounters resistance to movement. Once the motion initiated, the slide accelerates until, again due to resistance forces, it decelerates and eventually comes to a stop. This figure (left panel) shows that there is a time lag in the initial motion of the slide between the simulation and the experiment. The initiation of the motion is delayed in the simulation compared to the experiment. This delay decreases with the resolution though. If we omit this lag, and compare only the slope of the curves, then the prediction of the front displacement is approximately equivalent to the experimental data.

The hydrograph presented in Fig. 3 (right plot) also shows differences with the measurements while corresponding better to the theoretical model. The tendency is also to better match the data at higher resolution.

3.2. CASE 2: Wave generation and breaking

To evaluate the capacity of the model to generate a violent impulse wave, we considered the Jánosi et al. (2004) experimental test case. The experimental set-up is a wet dam break configuration (Fig. 4) resulting in a wave that breaks immediately as a plunging breaker. This case involves the interaction of two water masses with energy transfers from one mass to the other, followed by a complex free surface evolution during the breaking. As such, it involves similar processes as the ones usually acting during the generation of a wave by a sliding mass except that, here, there is no slope and the slide has the same physical properties as the water reservoir.

The experiment was carried out with three different downstream water levels (with the upstream water height $d_0 = 150$ mm): a dry case ($d = 0$), a rather shallow water case ($d = 18$ mm), and a deeper case ($d = 38$ mm). For validation purposes, we focused only on the deeper case. In order to reproduce the observed interface evolution, the motion of the gate had to be simulated as in Dumergue and Abadie (2022). Note that this gate motion has to be inferred as no law is given in the reference paper. In our study, the most precise results were obtained with a gate upward velocity set to 1 m/s. To simulate the gate motion, we implemented the `overInterDyMFoam` solver, a version of `interFoam` compatible with the over-set method (open source CFD toolbox, 2024). Note that with this code version, only two phases can be simulated. The mesh is uniform with a 5 mm square cell size for

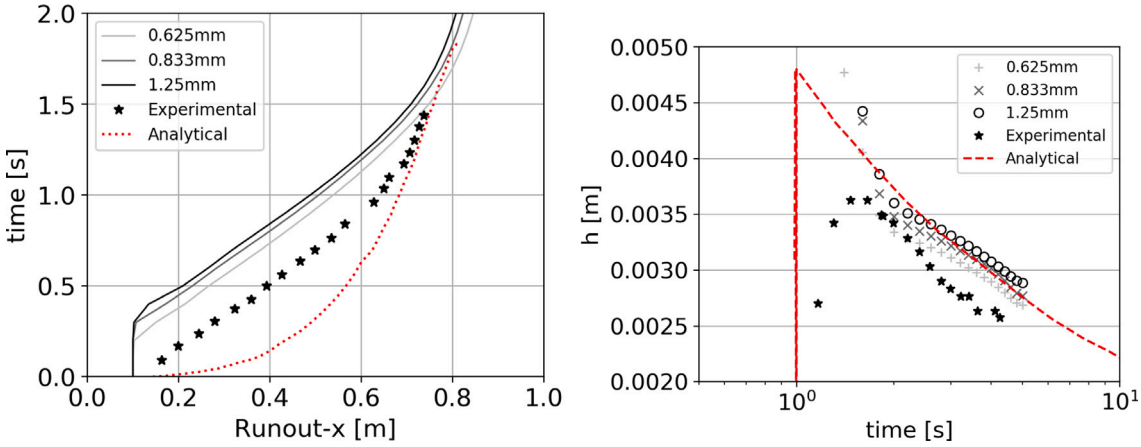

Fig. 3. Comparison of the simulation results with the experimental data and analytical solution of Huang and García (1998). Left: time evolution of the slide front position, Right: hydrograph at $x = 0.689$ m for the case (c) (Table 2).

the fixed domain and 2 mm cells in the dynamic mesh zone. In our simulation, we presumed the gate thickness to be equal to 5 mm. To ensure the gate is fully closed at the beginning, we defined a layer of impermeable porous medium at the bottom. This was necessary since usual wall boundary conditions cannot overlap with the gate contour at the beginning. We verified that this procedure does not influence the free surface evolution compared to a no-slip boundary condition. Finally, a turbulence model has been utilized with the same setup as the validation case described in Section 3.4.3.

Fig. 5 shows a comparison of the simulated and measured free surface location at different times. The correspondence is globally good at every stage of the wave generation process. The main wave breaking is, in particular, very well captured in the simulation. A notable discrepancy is nevertheless observed close to the gate at the very beginning of the simulation (first panel of Fig. 5). At this time, the first breaking caused by the returning wave is not particularly well captured by the model. This is likely due to the assumption made on the gate thickness and maybe also on the gate motion law which, both, affect directly this zone of the flow. In particular, a thinner gate may have produced a better result here, but this assumption has not been verified. There is also a slight discrepancy at $t = 0.406$ s, when the small breaking of a secondary wave, which occurs on the back of the main wave in the experiment, is not well reproduced by the model. In the simulation, a wave is formed ($t = 0.470$ s) but it is not energetic enough to break. This area of the flow corresponds to the back of the wave which was initially not well resolved by the model in the first panel. So again, the uncertainty on the gate thickness should explain this slight error.

We can infer from the preceding section that the breaking wave interface is accurately predicted by the two-phase model `interFoam`. However, usually, to simulate wave generated by landslide, a three-phase model is required (slide, water and air) such as `multiphaseInterFoam`. It is therefore important to also check the validity of the latter model. To do so, we repeated the Jánosi et al. (2004) case but without gate motion, as `multiphaseInterFoam` is not currently able to manage a dynamic mesh. The obtained results are compared to results obtained with the `interFoam` solver also without gate motion. Note that in the three-phase simulation, two phases are water and the third phase is air. Fig. 6 shows the comparison of the two model results. Obviously, they are very close to each other. Nevertheless, even though the problem solved is theoretically the same, a few slight discrepancies can be observed between the two model outputs, like the size of the air bubble entrapped for instance, or the rear part of the wave which is sharper in the three-phase case.

Table 3
Characteristics of the undular bores computed in this study.

Froude number	Upstream water level	Downstream water level
1.0104	0.3230 m	0.2510 m
1.1702	0.3685 m	0.2477 m

3.3. CASE 3: Wave dispersion — case of the undular bore

A wave generated by a subaerial landslide is generally nonlinear and dispersive. Moreover, in most of the cases, the leading wave exhibits dissipation by breaking. The last point will be investigated in more details in the next section. Here, we focus on the ability of the model to reproduce a non linear dispersive wave train. For that purpose, we simulated the generation of an undular bore with a wet dam break (Fig. 7) similar to the experiment described in Soares Frazao and Zech (2002). In this section, we considered two Froude numbers as indicated in Table 3.

We numerically re-constructed the two model setups and compared the water surface signals computed and measured at different gauge positions. The simulations were performed with the turbulence model of Devolder et al. (2017) to be consistent with the other test cases, but the influence of the latter is weak in this particular case (see Fig. 8 right panel). This is not surprising owing to the good results obtained in the same case with a fully nonlinear Boussinesq model without turbulence model (Tissier et al., 2011). Indeed, in this case, the capacity of the model to address the wave non linearity seems much more important than resolving the turbulent field.

A mesh sensitivity study is presented in Fig. 8 left panel for a particular Froude number with cells stretched in the horizontal direction. As can be observed, the model seems to converge but not to the measured data.

The finest mesh approximately covers the maximum wave height with ten cells and the horizontal cell dimension is stretched 10 times. Fig. 9 shows the comparison of the numerical results with the measurements obtained with this mesh. The model predicts the development of undulations at frequencies consistent with the measurements. Nevertheless, it also tends to underestimate the amplitude of these oscillations, especially for the larger Froude number.

Table 4 illustrates the relative errors of the simulated wave parameters. The comparison further highlights a higher relative error in the modeled wave height compared to the wave period. Finally, note that a comparison between the plots of Fig. 9 at x = 33.06 and x = 42.56 m,

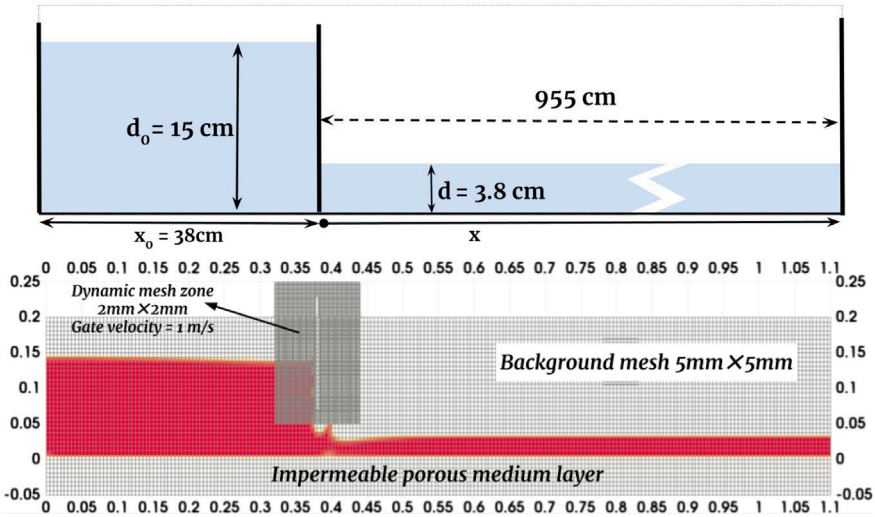

Fig. 4. Top: Schematic of the wet dam break setup (Jánosi et al., 2004) used for the model validation (dimensions are not in scale). Bottom: The computational domain and water condition at t = 0.07 s.

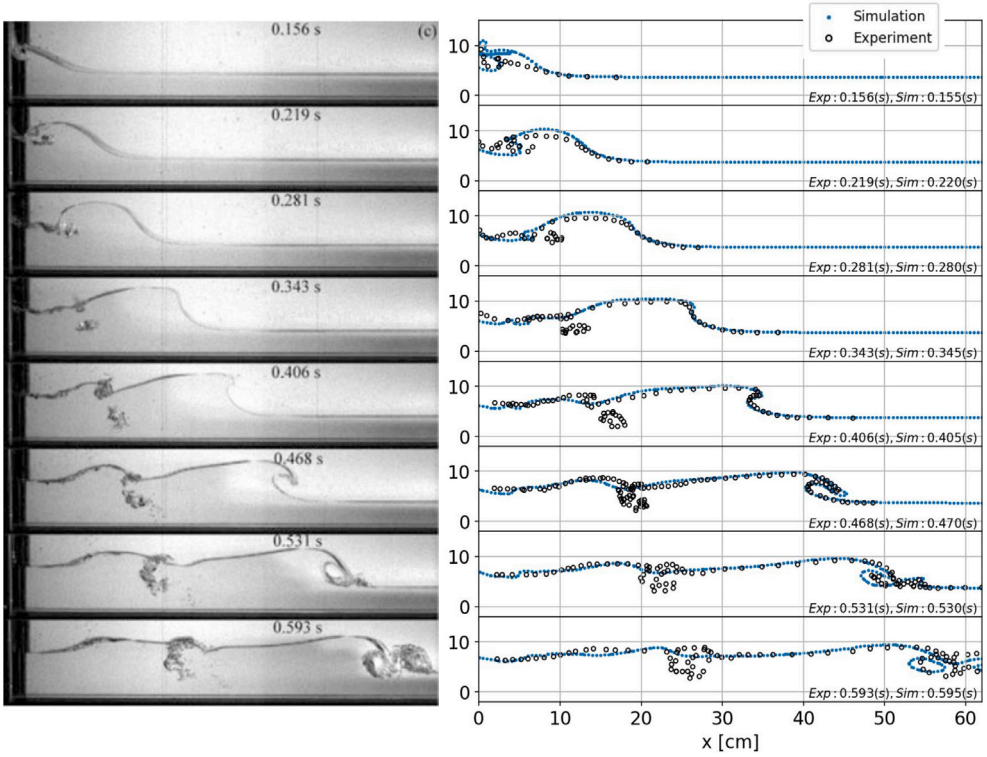

Fig. 5. Wave generated in a wet dam break. Left panel: sequences of experimental snapshots after releasing water, from Jánosi et al. (2004), right panel: free surface comparison between experimental and numerical results.

shows that the error on the first wave amplitude decreases with time as also shown in the table.

3.4. CASES 4 to 6: Validation of the energetic processes

Accurately simulating energy transfers in a wave generated by a subaerial landslide is a challenging task that requires the consideration of several complex processes. Theoretically, the initial slide potential energy progressively transforms into kinetic energy and, after the impact with the water surface, into wave kinetic and potential energy. During these processes, a fraction of this energy is dissipated, both from viscous (mainly associated with bottom friction and velocity gradients at the interfaces) and turbulent dissipation. The latter is mostly generated near the wave crest in wave breaking, either very violently (plunging breaking) or more gradually (in the turbulent bore case). During this process, some part of the mean flow kinetic energy is transferred to TKE. This process is the most important contribution to the

Table 4
Error assessment on H, wave height and T, period for the first two waves in the case Fr = 1.0104 at the different gauge positions for the most resolved case.

–	Exp	Sim	Difference	Exp	Sim	Difference	Exp	Sim	Difference
gauges	x = 33.06 m			x = 40.06 m			x = 42.56 m		
H_1	0.035 m	0.028 m	−20%	0.043 m	0.035 m	−17%	0.042 m	0.038 m	−9.5%
H_2	0.018 m	0.0168 m	−6%	0.025 m	0.021 m	−18%	0.0272 m	0.022 m	19%
T_1	1.19 s	1 s	−15.9%	1.108 s	1.178 s	+6.3%	1.19 s	1.23 s	2.7%
T_2	0.802 s	0.826 s	+3%	1.056 s	1.022 s	+3.25%	1 s	1.08 s	7.5%

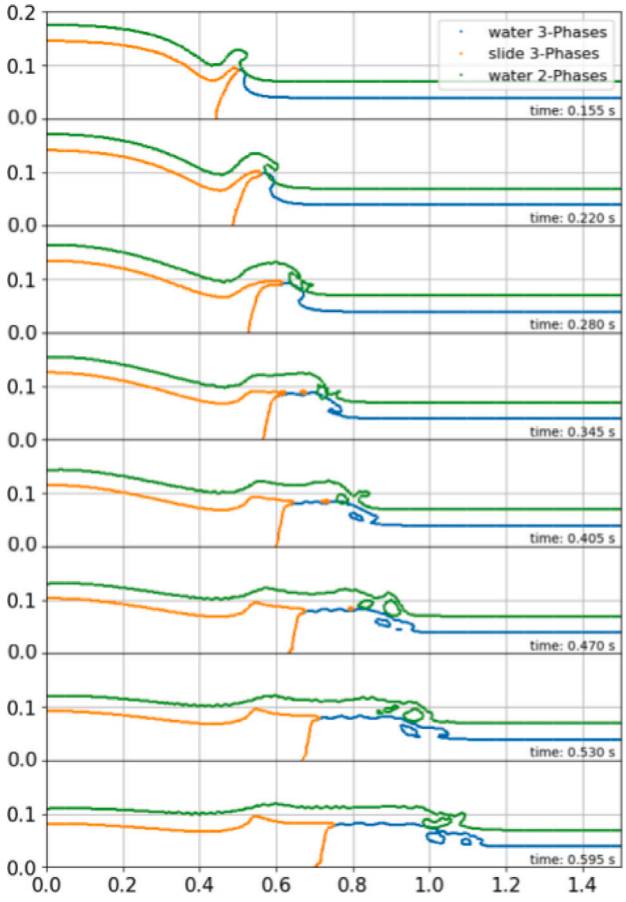

Fig. 6. Free surface comparison between two-phase `interFoam` and three-phase simulations `multiphaseInterFoam` for the same case as Fig. 5 but without gate motion simulation. Note that we applied a vertical offset of 5 cm to `interFoam` results in order to ease the comparison. Horizontal and vertical legend dimensions are in meters.

global dissipation (Eq. (24)). In this respect, finding the best turbulence model and the most suitable model configurations is imperative. This is one of the objective of this section. Another objective is to quantify the numerical dissipation of the model. Indeed, when investigating the energy processes, it is of great importance to ensure that the energy dissipation is due to actual physical processes and not to a numerical artifact. CFD models inherently suffer from numerical errors usually inducing significant diffusion. The objective of this part is at least to quantify and if possible minimize this numerical diffusion. The following sections present several validation test cases which address this general question of energy conservation and dissipation computation.

3.4.1. CASE 4: Energy conservation in a propagating solitary wave

The solitary wave is a common wave type appearing in the process of wave generated by a subaerial landslide (Fritz et al., 2004). It occurs generally after different wave transformation processes (i.e. dispersion and dissipation). In this case, the wave should be able to properly propagate without being artificially damped by numerical diffusion. The purpose of this section is therefore to control the conservation of energy for a propagating solitary wave over a flat bottom.

The computational domain, similar to the case studied in Wroniszewski et al. (2014), exhibits a length of 72.6 m, a height of 2.2 m and is discretized with square-shaped cells. The solitary wave is generated at the left boundary based on the formulation of Grimshaw (1970) (Fig. 10). The ratio of wave height to water depth H/h_0 is equal to 0.3 and the water depth (h_0) is 1 m. The bottom boundary condition is set to a free-slip condition to eliminate the viscous dissipation at the bottom.

The wave energy is the sum of the kinetic and potential components ($E_w = E_k + E_p$) described by Eqs. (21) and (23) with the y reference set at the initial water surface. The wave potential energy alternatively can be calculated by the water surface variation ($\eta(x)$) integration, as:

$$E_{p,w} = \frac{1}{2}\rho\, g \int \eta(x)^2\, dx \tag{29}$$

There are several sources of errors in this problem. We mention two of them here. The first one is the initialization of the water volume fraction. For instance, for three different resolutions (1056×32, 2112×64 and 4224×128, corresponding respectively to cell sizes of 68.8, 34.4 and 17.2 mm, with $\Delta x = \Delta y$), the error compared to the theoretical value of the water mass at$t = 0$ is 3.54, 0.31 and 0.30% respectively. The second error source comes from the progressive diffusion of the water volume fraction at the interface. Fig. 11 illustrates the effect of this artificial diffusion on the potential energy variation over time considering only the interface zone cells ($0.05 < \alpha_w < 0.95$) for the three previous tested resolutions on the same solitary wave case. The potential energy increases with an unacceptable rate in the case of the coarsest mesh resolution, while the finest resolution allows to keep a reasonable accuracy over time. Finally, the evolution of the wave energy components is presented on Fig. 12 for the finest mesh. Kinetic and potential energies are obviously stable over the 20 s computation (difference about 1%), which approximately corresponds to a propagation over about 10 equivalent wavelengths (Fig. 10).

In brief, the results demonstrate that, for a propagating wave, energy conservation can be ensured providing that sufficiently fine cells are used. In the case of the solitary wave, it was necessary to discretize the wave height with almost 20 cells to reach a satisfactory accuracy.

3.4.2. CASE 5: Energy conservation in a breaking solitary wave case

Most of the time, a subaerial landslide produces a large wave submitted to breaking. The dissipation is then either gradual, as in the turbulent bore or heterogeneous as in a violent plunging breaker. The present section focus on the last case by studying a solitary wave breaking over a slope. To the best of the authors knowledge, there are no theoretical values or measurements giving the amount of energy dissipated in this case. Therefore, the objective here is simply to quantify the error in the energy conservation equation (Eq. (28)) and try to minimize this quantity. The model setup, presented on Fig. 13, is similar to the experiment described in Li and Raichlen (2003). In this study, a solitary wave propagates over a 10 m flat bottom with a water depth (h_0) of 0.3 m. The initial wave height-to-water-depth ratio

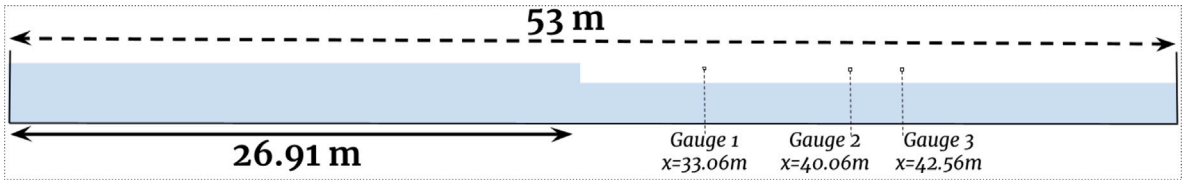

Fig. 7. Sketch of the undular bore generation set-up (Soares Frazao and Zech, 2002).

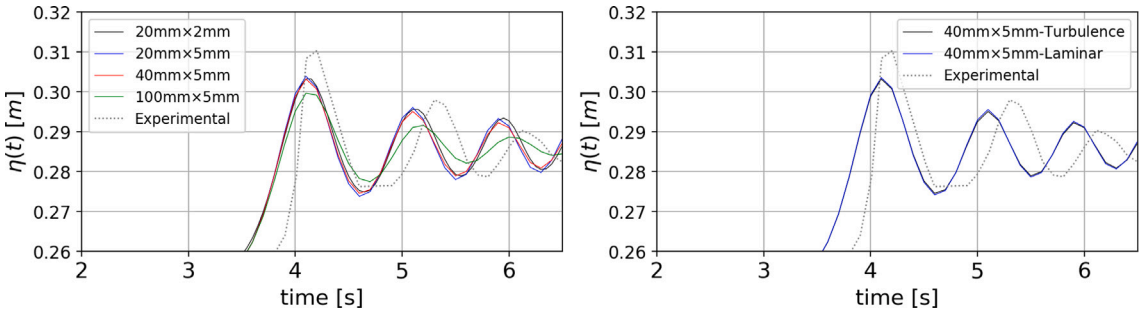

Fig. 8. Undular bore case (Fr = 1.0104). Left panel: comparison between the simulated free surface obtained with various mesh resolutions and the measurements of Soares Frazao and Zech (2002) (dotted line) at gauge position x = 33.06 m. Right panel: comparison between laminar and turbulent simulations — the two curves are perfectly superimposed.

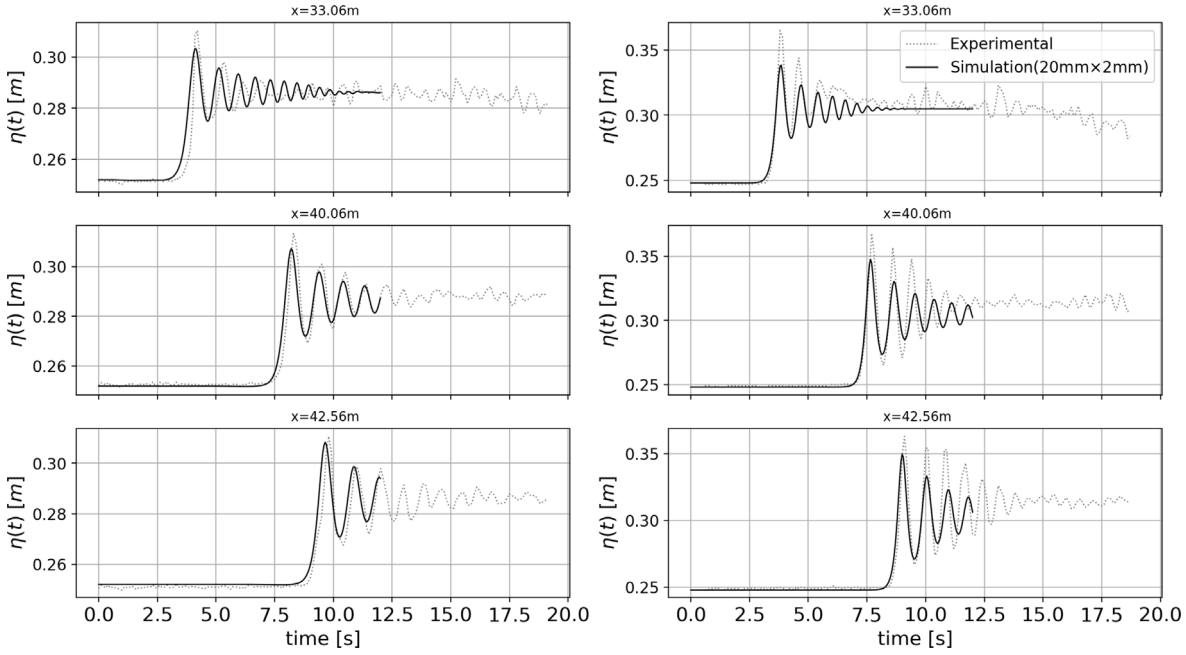

Fig. 9. Undular bore free surfaces for Fr = 1.104 (left panel) and Fr = 1.1702 (right panel) at different gauges positions.

is $H/h_0 = 0.3$. After the flat portion, the wave meets a 1:15 slope which induces the breaking and then the run-up of the wave.

The computational domain is made up of two adjacent blocks with the same number of rows and columns for the entire domain. The cell size is constant in the x-direction but gradually skews in the y-direction over the slope. Two meshes are considered here (i.e., $\Delta x = 2.5$ or 5 mm). The bottom boundary condition is a no-slip condition.

For this test case, the turbulence model plays a critical role in the energy balance through TKE and the TKE dissipation rate ϵ. All the turbulence models presented in Section 2.2 have been considered in the present study. Note that in this test case, the values of the initial turbulent parameters are not critical. Indeed, the time of wave propagation being long before the breaking, these parameters have sufficient time to converge to their physical values.

We first verified that the breaking is well reproduced by the model (Fig. 14). Fig. 15 next shows the time evolution of the different energy components. The wave energy dissipation starts to be non negligible above the slope and increases during the breaking and run-up. This dissipation is mainly due to turbulent processes. Note that during breaking, potential energy is transformed into kinetic energy while during run-up, the reversed process is observed.

Fig. 16 shows the comparison of the physical dissipation and the opposite of the total energy decrease for two different mesh resolutions 5 mm and 2.5 mm cell size.

The plot starts at $t = 5$ s when the wave is still propagating in the flat-bottom section and ends when the potential energy of the wave starts to decrease, at the end of the run-up. The difference between the two curves increases drastically during the mixing due to the violent breaking on the slope, in this case, the difference between the two

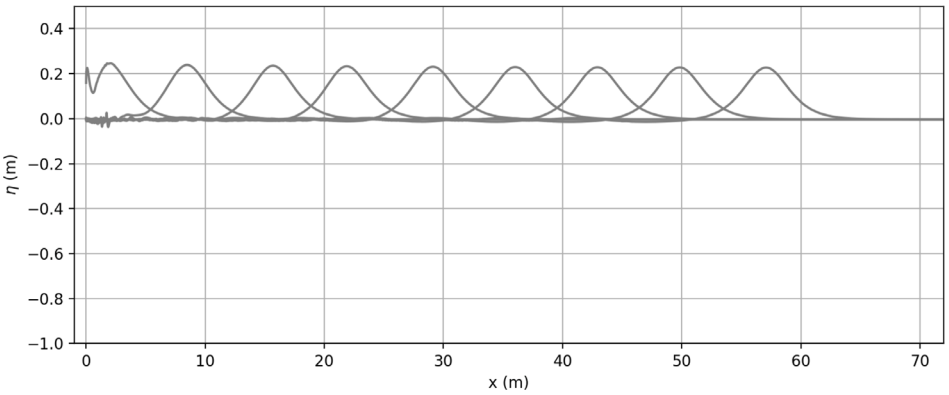

Fig. 10. Water surface at different times for a solitary wave initial profile with $H/h_0 = 0.3$. The mesh features 4224 × 128 cells. t = 0.1 s, 2.1 s, 4.1 s, 6.1 s, 8.1 s, 10.1 s, 12.1 s, 14.1 s, 16.1 s, 18.1 s from left to right.

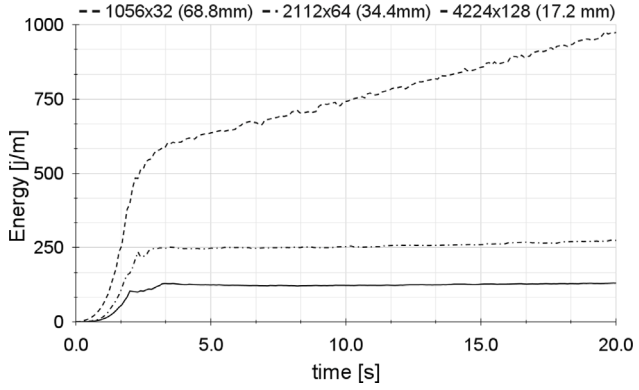

Fig. 11. Time variation of the water potential energy restricted to the interface cells ($0.05 < \alpha_w < 0.95$) for different mesh resolution.

curves, for 5 mm cell size model (Fig. 15), is 36% as detailed later in Table 5. During the run-up, energy is better conserved, as shown by a stable difference between the two curves. The comparison between the two plots (Fig. 16) indicates the significant influence of the cell size in achieving a better accuracy in the energy dissipation computation.

Table 5 provides a summary of the results regarding the conservation of energy for the different RANS turbulent models tested. The results show that only the modified $k-\omega$ SST and the $k-\epsilon$ RNG models are able to bound error in the energy balance equation (expressed in percentage of the initial wave energy) to reasonable values. For the first model (Devolder et al., 2017), the physical dissipation introduced in the turbulence model is lower than the decrease observed in the total wave energy. The decrease in the mesh size allows to reduce the error, as illustrated in Table 5, but it is obviously at the price of a heavier computation. The $k-\epsilon$ RNG also gives good results in this case, nevertheless, this performance was not reiterated in the other tests conducted (especially in the next section), conversely to the model of Devolder et al. (2017), and therefore, it was not retained. Finally, note that the model of Larsen and Fuhrman (2018) also gave good results for the present case (not shown in the table) but again less convincing than Devolder et al. (2017) in the next case.

3.4.3. CASE 6: Dissipation in a turbulent bore

In this section, we study the case of the dissipation of a turbulent bore, a frequent case appearing after a violent breaking of an impulse wave (Fritz et al., 2004). The bore is generated in a wet dam break process with the same set-up as in Yeh et al. (1989) and Mauriet (2009). The upstream reservoir height is 0.225 m and the downstream height is 0.0975 m (Fig. 17). The upstream reservoir is sufficiently large to ensure a steady propagation of the turbulent bore wave until the end of the downstream reservoir.

The turbulence model used here is the $k-\omega$ SST Buoyancy modified by Devolder et al. (2017). According to Mauriet (2009), the choice of the initial value of the turbulence model variables is important to represent properly the dissipation (especially if the propagation domain is short). We have conducted several tests to guess the optimal initial values for the model presently used. With k = 1e-4 [m^2 s^{-2}], ω = 1 [m^2 s^{-1}], and ν_t = 0 [m^2 s^{-1}], the model is found to provide reliable results. Note that these initial values mostly influences the beginning of the simulation and after a while the trend is the same whatever the initial values. The bottom boundary condition is a free-slip condition so that to restrain the dissipation to the breaking processes at the surface and therefore, be able to compare to the hydraulic jump theory. Finally, different uniform meshes are tested to study the influence of the resolution in the computation of the dissipation.

The theory of the turbulent bore generated in a wet dam break is described in Stoker (1992) (§10.6 and §10.8). The shock conditions written around the discontinuity, allows to compute the bore height h_m (Fig. 17) with:

$$\sqrt{h_1} = \sqrt{h_m} + (h_m + h_0)\sqrt{\frac{h_m + h_0}{8h_m \cdot h_0}} \tag{30}$$

In a coordinate system moving at the bore celerity, the flow is stationary. Several balance equations can be written. First, the mass conservation gives: $h_0 U = h_m(U-u)$, hence: $u = U\frac{(h_m-h_0)}{h_m}$. The momentum conservation reads: $\rho U^2 h_0 + \rho g\frac{{h_0}^2}{2} - \rho(U-u)^2 h_m - \rho g\frac{{h_m}^2}{2} = 0$, which gives: $U^2 = \frac{g h_m(h_m+h_0)}{2h_0}$. And finally, the variation of the flow energy through the discontinuity is: $\Delta E = \{\rho g h_0 + \rho\frac{U^2}{2}\} - \{\rho g h_m + \rho\frac{(U-u)^2}{2}\} = \rho g\frac{(h_m-h_0)^3}{4h_0 h_m}$ (J/m^3) by using the two previous results. Finally, multiplying by the flow discharge $U h_0$ gives the dissipation rate: $\Phi = \rho g U\frac{(h_m-h_0)^3}{4h_m}$ (J/s). With the current set-up, this yields to h_m = 0.154 (m), U = 1.4 (m/s), Φ = 4 (J/s). Therefore, in this case, conversely to the previous case, the physical dissipation is known theoretically.

Fig. 18 shows the results obtained with the model for the turbulent bore test case. In the inner subplot, we show that the simulated bore height matches the theoretical value, demonstrating that the macroscopic features of the flow are realistic. The bottom panel displays the dissipation computed by the model and the opposite of the energy decrease for different mesh resolutions. The difference between the continuous and the associated dotted lines gives ΔE_{error} for the given resolution. This plot shows that the error keeps reasonably bounded for all the simulations but especially for the finer mesh. Moreover, after a transitional regime in the beginning of the simulation (i.e., the first 1.5 s), the dissipation rate calculated by the model (i.e., the slope of

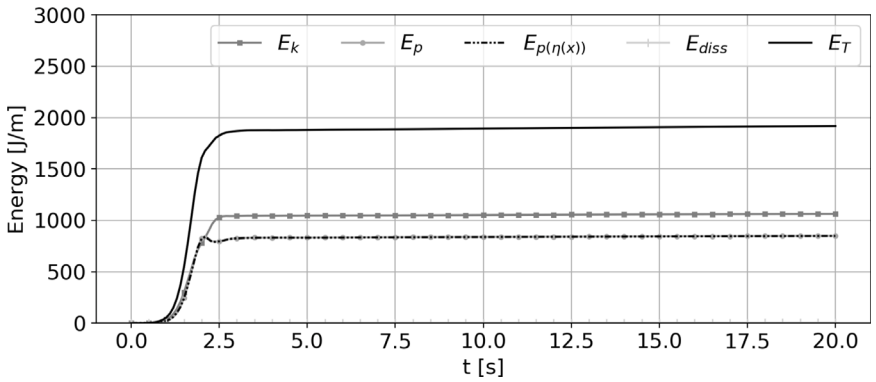

Fig. 12. Time evolution of the energy components for the propagating solitary wave case of Fig. 10 and the finest mesh resolution. Solid black line: wave total energy ($E_p + E_k$); grey line with □ mark: wave kinetic energy (E_k) (Eq. (21)); grey line with ∘ marks: wave potential energy E_p calculated with Eq. (23); dash-dotted line: wave potential energy calculated from the extracted water interface $\eta(x)$ (Eq. (29)); '+': Energy dissipation (negligible in this case).

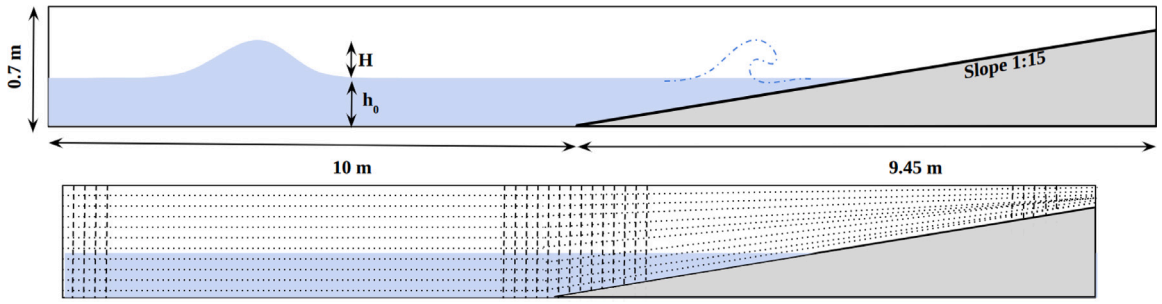

Fig. 13. Top: Schematic view of the breaking solitary wave test case (the sketch dimensions are not in scale). Bottom: Sketch of the cells arrangement. The meshes used are: 3890 × 140 and 7780 × 280, respectively corresponding to a cell size of 5 mm and 2.5 mm.

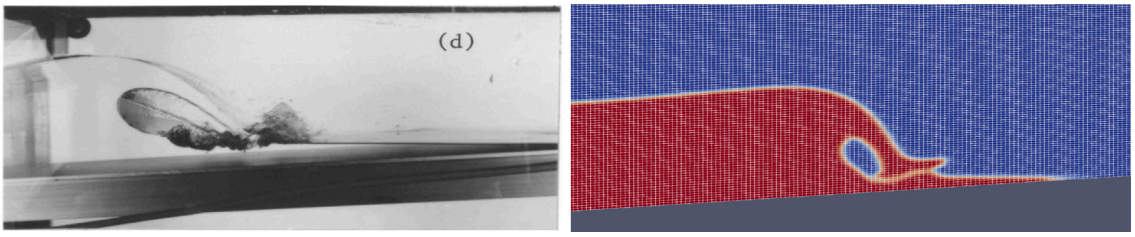

Fig. 14. Comparison of the breaking wave shape between the experimental data of Li and Raichlen (2003) (left) and the simulation (right). The simulation is carried out with the $k-\omega$ SST turbulence model of Devolder et al. (2017).

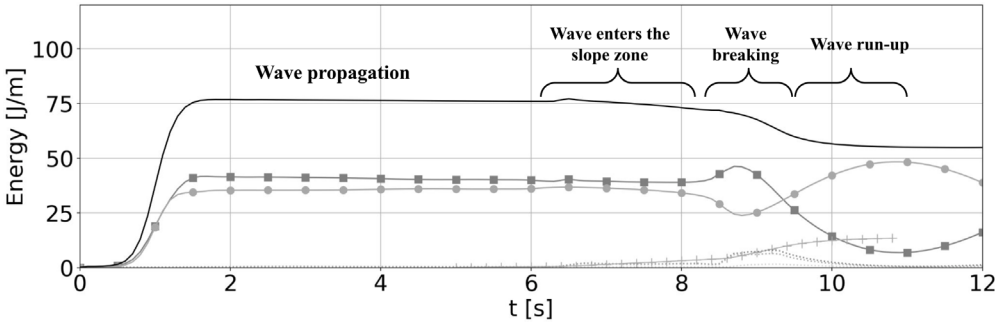

Fig. 15. Time evolution of the wave energy components in the breaking solitary wave case. The simulation is performed with the $k-\omega$ SST buoyancy modified turbulence model of Devolder et al. (2017). The cell size = 5 mm. solid line: $E_k + E_p$, grey line with ∘: E_k, grey line with □: E_p, and grey line with "+": integrated dissipated energy.

the curve) correspond to the theoretical value; the resolution gradually improving this assertion.

Finally, Table 6 gives the values of the dissipation and the opposite of the energy decrease for different other turbulence models tested in this case for comparison with the model of Devolder et al. (2017) at time t = 4 s. This table clearly shows the better performance of the latter model compared to the others in terms of energy conservation as well as for an accurate estimation of the actual dissipation.

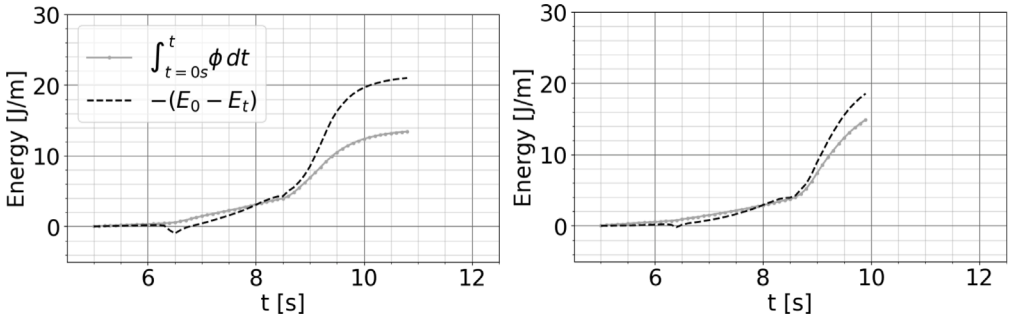

Fig. 16. Comparison between the direct computation of the physical energy dissipation (grey line with ∘) and the decrease in total wave energy (black dash line) for the case of Fig. 15. Note that the last curve has been artificially multiplied by −1 to allow a direct comparison. Left panel: for the 5 mm cell size test case, Right panel: same graph for the 2.5 mm cell size test case.

Table 5
Solitary breaking wave test case — Energy conservation error for the different RANS models tested.

Turbulence model	Cells size	$E_{start} - E_{end}$	$\int_{t=5s}^{t_{max-runup}} \phi\, dt$	Energy conservation error (ΔE_{error}) (%)
$k-\omega$ SST (Devolder et al., 2017)	2.5 mm	18.6	15.1	19
$k-\omega$ SST (Devolder et al., 2017)	5 mm	21.01	13.4	36
$k-\omega$ SST	5 mm	11.13	37.57	−238
$k-\epsilon$ RNG	5 mm	21.47	15.68	27
$k-\epsilon$ Non-linear	5 mm	5.6	60	−971
standard $k-\epsilon$	5 mm	8.8	55.35	−529

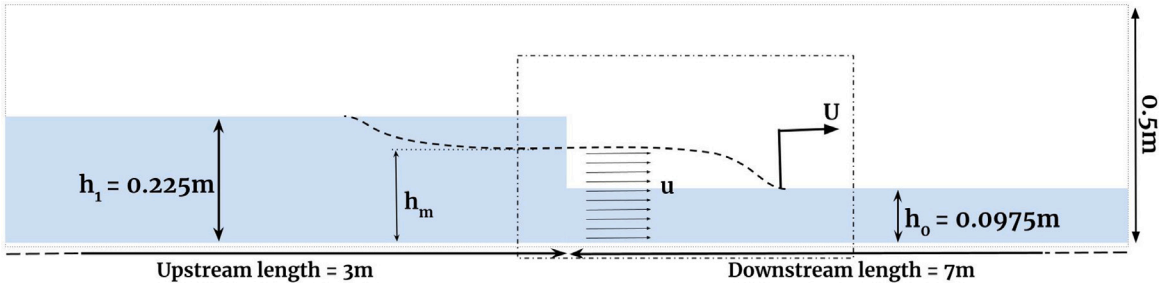

Fig. 17. Initial condition and physical parameters in the progressive turbulent bore case (dimensions are not in scale).

Table 6
Opposite of total energy decrease and energy dissipation at t = 4 s for the different RANS models tested in the turbulent bore case. At this time the theoretical energy dissipation is 16 [J/m].

Turbulence model	Cells size	$E_0 - E_{t=4s}$	$\int_{t=0s}^{t=4s} \phi\, dt$	ΔE_{error} (%)
$k-\omega$ SST (Devolder et al., 2017)	2 mm	14.89	13.93	−6.4%
$k-\omega$ SST (Devolder et al., 2017)	5 mm	13.62	11.89	−12.7%
$k-\omega$ SST(Larsen and Fuhrman (2018))	5 mm	13.87	8.55	−38.35%
$k-\epsilon$ RNG	5 mm	12.33	23.07	87%
$k-\omega$ SST	5 mm	7.78	36.76	372%
standard $k-\epsilon$	5 mm	9.41	32.71	247%

4. Discussion

4.1. Significance of the results

In this paper, we have simulated several test cases to assess the capacity of the `interFoam` and `multiphaseInterFoam` solvers to reproduce the important physical processes involved in the generation of wave by subaerial landslides. Our approach was to decompose the work in elementary processes occurring sequentially in the global phenomenon. Additionally, we focused particularly our effort on the energy transfers which, to the best of the authors knowledge, are rarely addressed in the literature at the stage of the model validation.

We first simulated a non-Newtonian slide flow. With the same model, Rauter et al. (2021) found a large discrepancy on the slide thickness between the model and the experiment (Bullard et al., 2019) for a water slide while the velocity was better reproduced. Our results show a better match for the slide shape even though some differences are observed especially in the immediate rear part of the slide front. As in Rauter et al. (2021), the slide velocity is correctly captured by the model. Note that in Rauter et al. (2021), the cell size is 1 cm and the slide thickness ranges from 3 to 7 cm, which gives between 3 to 7 cells in the slide thickness. The same kind of resolution or a little finer is used in our study (see first line column 4 of Table 1). We can guess that the case simulated in Rauter et al. (2021) is harder to reproduce due to the long distance of slide flow before water impact and thus the higher velocity acquired by the slide (i.e., around 6 m/s against 1.5 m/s in our case). Interestingly, this case does not require many cells in the slide thickness to obtain acceptable results. Nevertheless, as often with this type of model, a higher resolution does not necessarily means better results. This is often due to the gradual appearance of low-scale physical processes when increasing resolution, which would need even higher resolution to be correctly accounted for (such as here

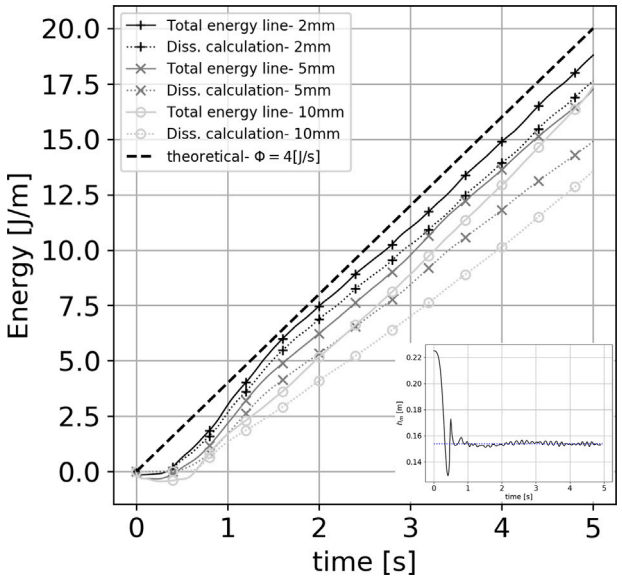

Fig. 18. Comparison between the simulated dissipation –dotted lines– and the opposite of the energy decrease –solid lines– with the expected theoretical value –dashed line– for different cell resolutions. Inner subplot: Comparison of the simulated (2 mm) bore height (taken 60 cm behind the bore front) –solid black line– with the expected theoretical value — blue dashed line.

Kelvin–Helmholtz instabilities for instance) or additional physics to be included in the model.

The generation of the impulse wave in a wet dam break configuration (Jánosi et al., 2004) showed the sensitivity of the breaking wave shape to the interaction between the two fluid masses. Indeed, in this case, the simulation of the lift gate velocity was required to reproduce the experimental wave shape. This emphasizes the importance of an accurate modeling of the slide shape and velocity when the latter impacts water in a subaerial landslide wave simulation. Indeed, the slightest errors in these parameters are immediately transferred to the subsequent wave breaking motion and thus, to the energy dissipation.

For the undular bore case, if correct results were obtained for the oscillations periods, the amplitudes of the oscillations were underestimated. In this case, the model results seem to converge when increasing the resolution but not to the experimental measurements. Our interpretation of this result is that the VOF algorithm may have difficulties to solve the initial instant of the dam break especially due to the presence of a corner in the water phase (Aulisa et al., 2003). This is actually a difficult case for this type of method and this difficulty may explain the loss of amplitude observed in our results. Due to that, this case may not be the most relevant to test wave dispersion. Additionally, the following case (Section 3.4.1) involving the propagation of a solitary wave over long distance shows very satisfactory results in terms of amplitude and energy conservation. This is an encouraging results for the use of this type of model for long distance wave propagation (as needed in our case). A solitary wave being stable under the balanced effects of nonlinearities and dispersion, this also shows that these affects are correctly reproduced in the model, modulating a bit the negative results of the preceding case.

The case of the solitary wave breaking shows first the importance of the mesh size on the global energy conservation (Fig. 16). This is expected as the numerical dissipation associated to the discretization of the convective terms is a function of the cell size. For instance, the use of the UPWIND scheme deteriorate totally the solution and, with this scheme, the difference between the dissipation and the energy decrease is unacceptable. Nevertheless, Table 5 shows an even greater influence of the turbulence model on the energy conservation error. This is also expected as both, the kinetic turbulent energy k and the turbulent dissipation ϵ appear on each side of Eq. (27). Therefore, any inconsistencies in the turbulent model should appear in the energy conservation error. Research on wave breaking simulation has already shown the importance of the turbulence model (Devolder et al., 2018; Li et al., 2022). For instance, studying wave breaking with a RANS model and a $k-\epsilon$ model, Lin and Liu (1998) found that the turbulence levels near the breaking point were significantly overestimated compared to the experimental data. As a consequence, energy dissipation was responsible for under prediction of the breaking wave height. Since then, this observation has been consistently reported (Christensen, 2006; Fernandez-Mora et al., 2017; Xie, 2013) and it was the main reason for the introduction of the buoyancy term in the model proposed by Devolder et al. (2017). Table 5 shows that this additional term allows globally a better energy conservation. Additionally, the last case featuring the turbulent bore shows that, with this turbulence model, the level of the turbulent dissipation is approximately the one theoretically expected. Note that Reynolds stress turbulence modeling also appears as a very promising model for this type of flow, as shown in the recent work of Li et al. (2022). Owing to the performance of this model, testing it with respect to energy conservation, as done for other models in the present work, would be very interesting.

4.2. Waves generated by subaerial landslides: Examples of simulation

The aim of this section is to show how the energy conservation problem pointed out in the result section, manifests itself in actual simulations of waves generated by a subaerial landslide. We propose here two simulation cases. In the first one, the slide initially starts at the free surface (Viroulet et al., 2014), therefore the initial potential energy is moderate. The second slide case stands initially at a much higher elevation, leading to significant transfers of energy and dissipation. For the two cases considered, two turbulence models are used, namely, the standard $k-\omega$ SST model and the $k-\omega$ SST buoyancy modified by Devolder et al. (2017).

4.2.1. Moderately energetic case

The first case considered is the subaerial granular landslide studied in the experiment of Viroulet et al. (2014). The landslide is composed of 0.0015 m diameter glass beads, contained in a 0.11 m high isosceles right-angled triangle by a vertical plate. The granular material, initially just above the free surface, flows over a 45° slope when the gate is released. The depth h_0 is equal to 15 cm. The evolution of the collapse was recorded by a high speed camera and the wave train was followed thanks to four resistive gauges located at 0.45, 0.75, 1.05 and 1.35 m from the plate.

The numerical model set-up corresponding to the experiment is presented in Fig. 19. The mesh is uniform with $\Delta x = \Delta y = 2.5$ mm (i.e., 127920 cells). This gives about 12 cells in the maximum wave amplitude (i.e., about 3 cm) according to the data of Viroulet et al. (2014) (see Fig. 20) and about 20 cells in the slide thickness. We shall show later that this resolution is sufficient to achieve a correct accuracy owing to the low energy dissipation involved in this case.

The equivalent density of the slide was evaluated to approximately 1900 kgm^{-3}, assuming that the voids between the grains are filled completely with water. The simulation is performed with a Newtonian slide. The equivalent viscosity of 10 Pa s corresponds to the average value, a $\mu(I)$-rheology granular model (Jop et al., 2006) would give for this specific slide (Clous and Abadie, 2019). Note that, obviously, the Newtonian rheology does not reproduce perfectly the phenomenon and especially, here, the penetration of water within the grain during the slide interaction with water. This leads to a slower simulated slide compared to the experiment (Clous and Abadie, 2019; Paris et al., 2021), with a discrepancy increasing with time. Nevertheless, Clous and Abadie (2019) showed that, as the energy transfers are very quick in this case, this discrepancy in the slide motion does not really has time to affect the waves generated (Fig. 20).

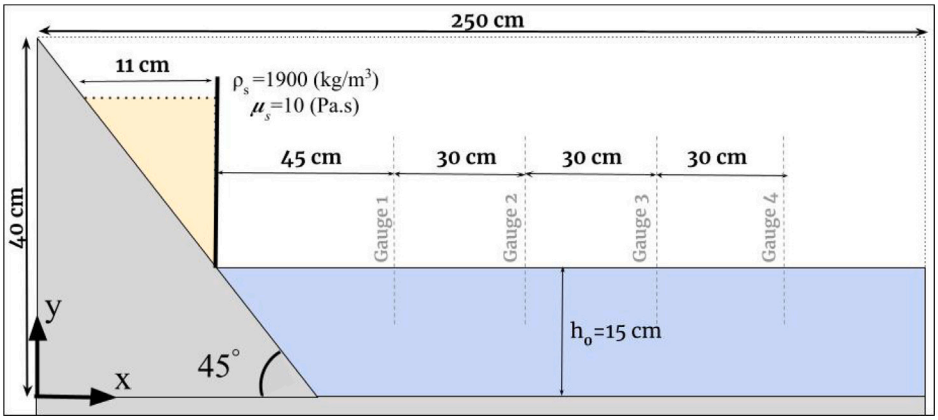

Fig. 19. Schematic view of the numerical model setup at$t = 0$ based on the experiment of Viroulet et al. (2014).

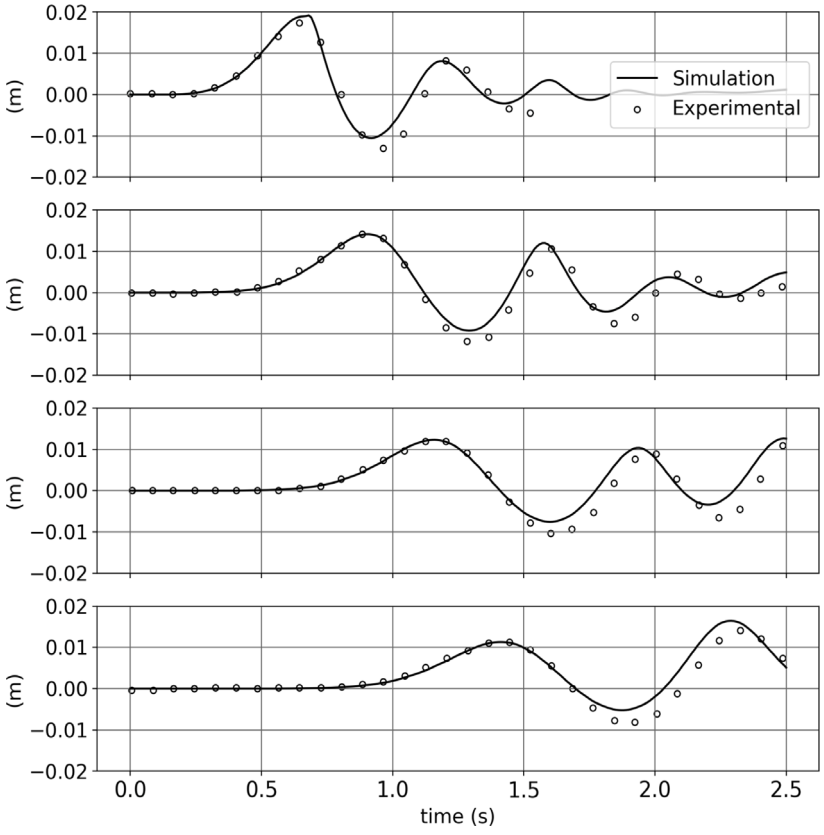

Fig. 20. Comparison between the free surfaces computed and measured at the four gauge positions in the case of Viroulet et al. (2014). Here the simulation has been performed with the $k-\omega$ SST buoyancy modified (Devolder et al., 2017).

Fig. 21 shows the snapshots of the computed slide and water interfaces and the streamlines at different instants of the wave generation process. Here, as in the experiment, the wave generated does not really break, or only for a very brief instant.

Fig. 22 shows the behavior of the model in terms of energy conservation. In this case, both turbulence models give satisfactory results. The dissipation occurs essentially in the slide but even there it is relatively limited. In water, the dissipation is negligible as there is no wave breaking. So we can conclude that when dissipation is limited, the mesh resolution and the choice of the turbulence model are not really critical.

4.2.2. *Strongly dissipative case*

In this case, the slide surface (same shape as previously) is much larger than in the previous case ($h_s = 2h_0$ against $h_s = 0.73h_0$ in the previous case, with h_s slide side length). Additionally, the slide initial elevation (i.e., the distance from the slide bottom to the water level) is now $2.5h_0$ with h_0 equal to 0.2 m (against 0 previously). This, along with the larger surface, lead to a much stronger interaction with the water free surface and a significant dissipation, globally speaking. Note also that, conversely to the previous case, there is no data to validate this simulation.

The slide considered is a non-Newtonian fluid following the Herschel–Bulkley law (rheological parameters: $\tau_0 = 9.96$ [Pa], $n = 0.38$,

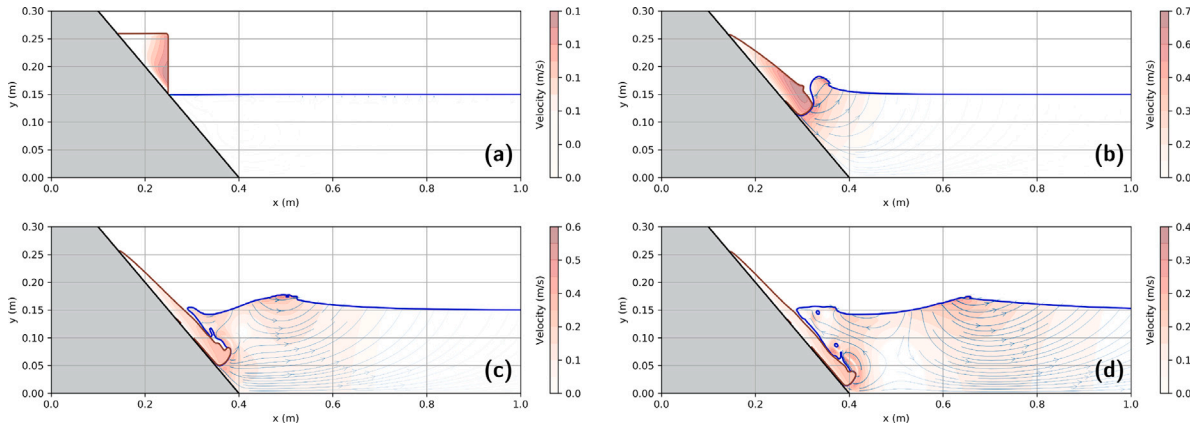

Fig. 21. Fluid interfaces, streamlines and velocity magnitude (surface field) at different times in the case of Viroulet et al. (2014). a: t = 0.01 s, b: t = 0.2 s, c: t = 0.4 s, d: t = 0.6 s. The turbulence model is the $k-\omega$ SST buoyancy modified (Devolder et al., 2017).

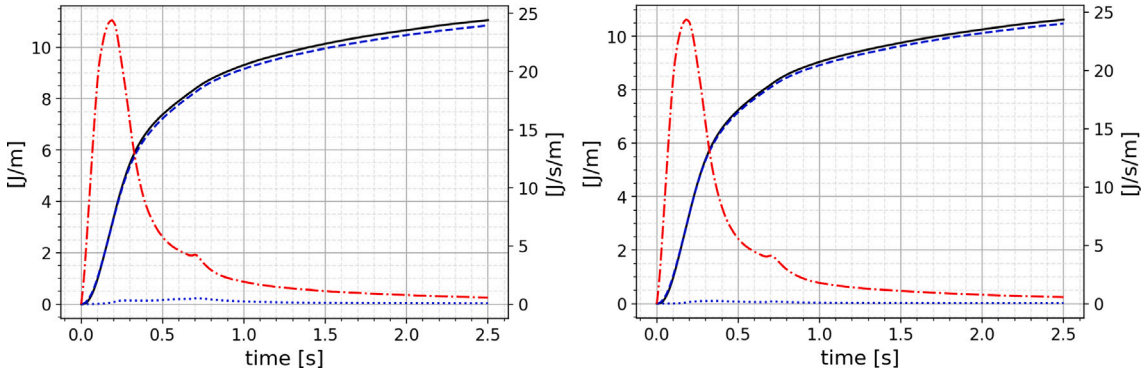

Fig. 22. Energy conservation in the system in the case of Viroulet et al. (2014) with the standard $k-\omega$ SST model (left) and the $k-\omega$ SST buoyancy modified (Devolder et al., 2017) (right). Solid black line: Total energy line drop, Dashed blue line: energy dissipated in water and slide (values correspond with the left axis). Dotted blue and dash-dotted red lines: dissipation rate in water and slide phases respectively (values corresponds with the right y-axis).

$K = 7.1$ [Pa s^n]). This makes the link with the first validation case considered in this paper. With the present parameters, the slide is highly mobile.

The channel is 20 m long and the slope 45°. The mesh has 834800 cells with $\Delta x = \Delta y = 5$ mm. With this cell size, the maximum slide thickness (Fig. 23, first row) is discretized with 15 cells, the breaking wave amplitude (Fig. 23, row panel) with 48 cells and the bore wave amplitude (Fig. 23, fourth row) with 27 cells.

Fig. 23 shows the sequences of the flow simulated with the two turbulence models. This figure illustrates all the individual processes considered earlier in the paper. For instance, in the top row, the slide is flowing over the slope (validation case of Section 3.1). On the row just under, there is a strong interaction between the slide and the water interfaces (validation case of Section 3.2), leading to a breaking wave in the third panel. Finally, the two bottom rows show the complex dynamic affecting the wave, with breaking (first plunging (validation case of Section 3.4.2) then spilling (validation case of Section 3.4.3)), dispersion (validation case of Section 3.3) and non linear effects acting during the propagation over relatively long distance (validation case of Section 3.4.1). We note that the results obtained with the two turbulence models are not very different if we consider the water and slide interfaces. The shape of the leading wave is just slightly different at t = 5 s.

The preceding remark is no longer valid when considering energy conservation (Fig. 24). This time, the results obtained with the two turbulence models are critically different. With the standard $k-\omega$ SST model, energy is not conserved. The physical dissipation is much larger than the corresponding decrease in the total energy of the system. Whereas the energy decrease is approximately the one obtained with the other turbulence model in accordance with the similarity of the results noted in Fig. 23. This likely means that the turbulent dissipation ϵ is too large in the standard $k-\omega$ SST model. Indeed if we compare the dissipation peaks reached in the slide and water, the relative difference between the two models is 166% for the first one, and 600% for the second one. This difference is obviously not acceptable when addressing the problem of energy transfer from slide to waves.

4.3. Limitations of the study

In this paper, we have presented a validation of the OpenFOAM multiphase solver with respect to elementary processes identified as generally occurring in the problem of waves generated by subaerial landslides. By splitting this problem in separated element, our objective was to put a stronger focus on each process, compared to usual validation works proposed on the same subject and therefore, better understand the model set-up requirement in each case. This approach does not replace an actual validation of the code considering the global problem (i.e., a wave generated by a landslide), but rather complete such a validation. Indeed, in our work, the processes are considered individually (which is also the interest of the study) while, in the global problem, they interact non linearly. Additionally, all the validation cases considered in this work, are simulated with the solver `multiphaseInterFoam` except for one, the case of Jánosi et al. (2004), which was resolved with `InterFoam`. The use of different solvers can make a difference when dealing with the global problem. Nevertheless, for this case, we provided a comparison of both solvers to show that they behave very similarly. Other limitations are obviously

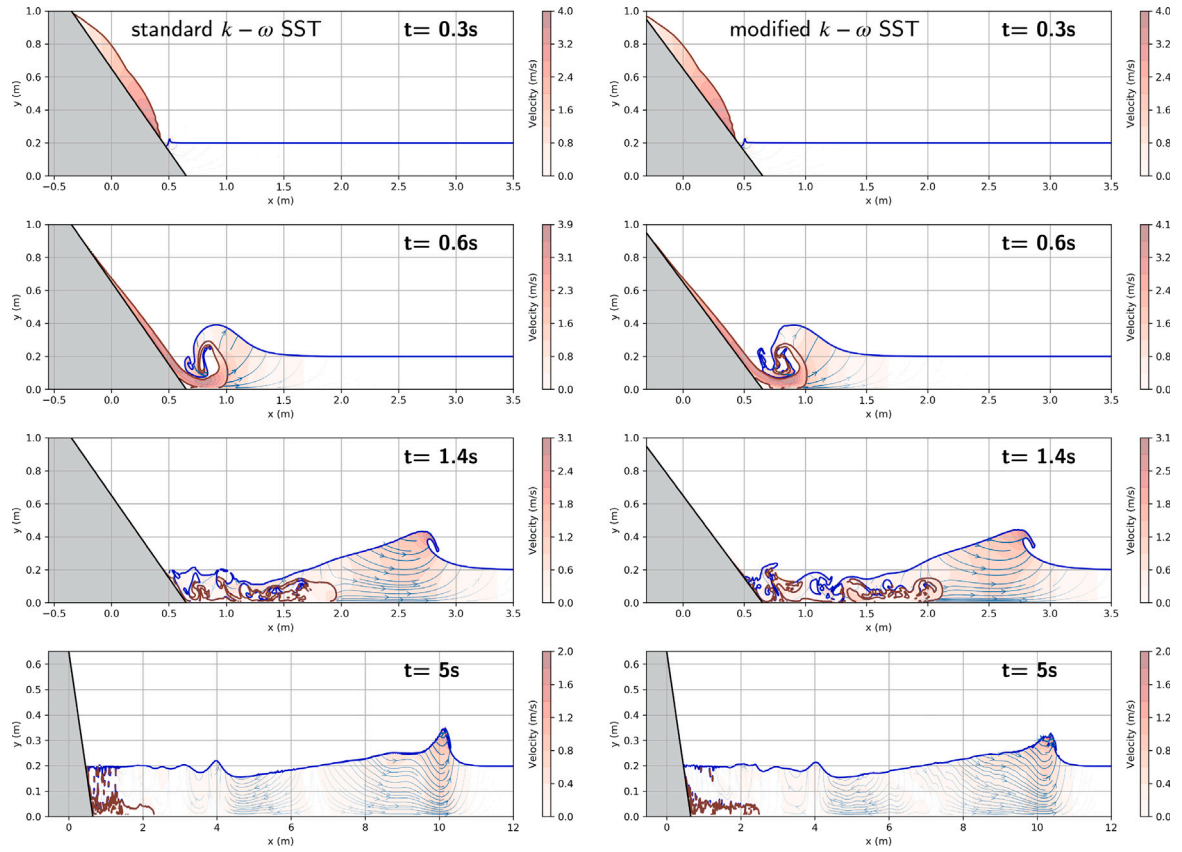

Fig. 23. Fluid interfaces, streamlines and velocity magnitude (surface field) at different times (top to bottom: t = 0.3 s, 0.6 s, 1.4 s, 5 s) for a non-Newtonian slide case that generates an impulse wave for two turbulence models. Left column: standard $k-\omega$, right column: $k-\omega$ SST buoyancy modified by Devolder et al. (2017).

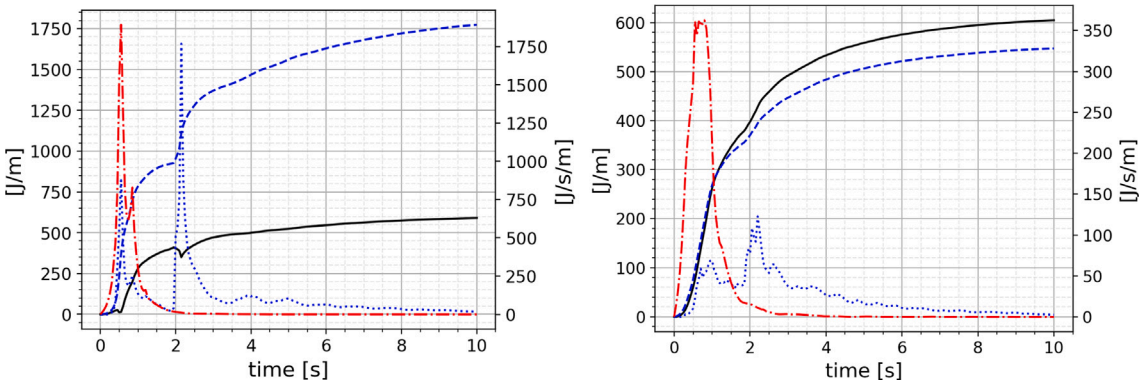

Fig. 24. Energy conservation in the model over time for the case of Fig. 23 for two different turbulence models. Left panel: standard $k-\omega$, right panel: $k-\omega$ SST buoyancy modified (Devolder et al., 2017). The legend description is similar to Fig. 22.

the simplification of the slide rheology, the absence of a slope in the generation case and, more globally, the omission of the third dimension in the simulations. Finally, note that for a validation of the `multiphaseInterFoam` code for wave generated by high mobility subaerial landslide (like in Fig. 23), the reader is referred to the work of Rauter et al. (2021). The set-up of the model proposed in the example of Fig. 23 is very similar to the one of Rauter et al. (2021) in terms of mesh size and time step control (i.e., the requirement of a very low CFL value). Therefore, we may expect comparable accuracy as achieved in this work.

5. Conclusions

Our study provided a comprehensive validation of the model OpenFOAM (i.e. essentially `multiphaseInterFoam`), with respect to several important processes involved in waves generated by subaerial landslides including: landslide flow, wave generation by liquid phases interaction, wave breaking inception and wave dispersion. The following conclusions can be drawn from this extensive work:

- The non-Newtonian slide flow shape and velocity are resolved with an acceptable accuracy with a limited number of cells in

the vertical direction (around 5). A slight discrepancy in the slide front shape is nevertheless to be expected with this resolution.
- The generation of an impulse wave and the subsequent breaking were correctly reproduced in a wet dam break case, with about 10 cells along the breaking wave height but required a fine tuning of the model (i.e., the gate motion) to reproduce the wave shape. This shows the sensitivity of this model to the conditions of the interaction of the two masses.
- Dispersion processes were investigated through the case of the undular bore generation. With comparable resolutions as in the previous validation cases, the numerical results did not vary significantly with the mesh size and the error was not negligible especially for the wave height. The main frequency of the wave train was more correctly reproduced.

Energy conservation and dissipation computation, two aspects largely overlooked in the literature, were also investigated for the solitary wave and the turbulent bore cases. It was shown that:

- the use of a fine mesh (along with an appropriate scheme for the discretization of the convective terms, like here the linear UPWIND scheme) is mandatory to reduce numerical dissipation. But with the CFL constraints, this increases substantially the CPU time. Therefore a compromise had to be found. Accordingly, with 20 to 25 computational cells over the wave height, the conservation of energy is approximately satisfied and the computation of the dissipation has an acceptable accuracy,
- for the solitary wave breaking case, the conservation of energy was shown to strongly depend on the turbulence model. Only the use of the $k-\omega$ SST buoyancy modified turbulence model (Devolder et al., 2017) was able to ensure the energy conservation. The other models such as the standard $k-\epsilon$ lead to unacceptable unbalance in the energy conservation. The initial conditions for the turbulence model variables were also shown to influence the energy computation. Hence, with the appropriate values, the energy dissipation is shown to be accurately simulated in the turbulent bore case.
- Finally, the model has been applied to two cases of waves generation by subaerial landslides. The case involving moderate initial slide energy was found to be relatively insensitive to the choice of the turbulence model (i.e., standard or buoyancy modified $k-\omega$ SST) in terms of energy conservation. Nevertheless, the conclusions were drastically different when significantly larger slide energy was considered. In this case, the use of the buoyancy modified $k-\omega$ SST turbulence model was found mandatory to ensure energy conservation and accurate dissipation computation.

CRediT authorship contribution statement

Amir H. Parvin: Writing – review & editing, Writing – original draft, Visualization, Validation, Software. **Stéphane Abadie:** Writing – review & editing, Writing – original draft, Validation, Supervision, Conceptualization. **Kamal El Omari:** Writing – review & editing, Validation, Supervision. **Yves Le Guer:** Writing – review & editing, Supervision, Project administration, Funding acquisition.

Declaration of competing interest

The authors declare the following financial interests/personal relationships which may be considered as potential competing interests: Amir H. Parvin reports financial support was provided by Nouvelle-Aquitaine Regional Council. If there are other authors, they declare that they have no known competing financial interests or personal relationships that could have appeared to influence the work reported in this paper.

Acknowledgment

Amir Parvin's PhD grant was funded by the Nouvelle Aquitaine Region through the TerraNAmi project (Grant No. 2019-1R20131).

References

Abadie, S., Morichon, D., Grilli, S., Glockner, S., 2010. Numerical simulation of waves generated by landslides using a multiple-fluid Navier–Stokes model. Coast. Eng. 57 (9), 779–794.

Abadie, S., Paris, A., Ata, R., Le Roy, S., Arnaud, G., Poupardin, A., Clous, L., Heinrich, P., Harris, J., Pedreros, R., Krien, Y., 2020. La Palma landslide tsunami: calibrated wave source and assessment of impact on French territories. Nat. Hazards Earth Syst. Sci. 20 (11), 3019–3038.

Aulisa, E., Manservisi, S., Scardovelli, R., 2003. A mixed markers and volume-of-fluid method for the reconstruction and advection of interfaces in two-phase and free-boundary flows. J. Comput. Phys. 188 (2), 611–639.

Basu, D., Das, K., Green, S., Janetzke, R., Stamatakos, J., 2010. Numerical simulation of surface waves generated by a subaerial landslide at Lituya Bay Alaska. J. Offshore Mech. Arct. Eng. 132 (041101).

Battershill, L., Whittaker, C.N., Lane, E.M., Popinet, S., White, J.D.L., Power, W.L., Nomikou, P., 2021. Numerical simulations of a fluidized granular flow entry into water: Insights into modeling tsunami generation by pyroclastic density currents. J. Geophys. Res.: Solid Earth 126 (11), e2021JB022855.

Beverly, C., Tanner, R., 1992. Numerical analysis of three-dimensional Bingham plastic flow. J. Non-Newton. Fluid Mech. 42 (1), 85–115.

Bilal, M., Xing, A., Zhuang, Y., Zhang, Y., Jin, K., Zhu, Y., Leng, Y., 2021. Coupled 3D numerical model for a landslide-induced impulse water wave: A case study of the Fuquan landslide. Eng. Geol. 290, 106209.

Biscarini, C., 2010. Computational fluid dynamics modelling of landslide generated water waves. Landslides 7 (2), 117–124.

Bougouin, A., Paris, R., Roche, O., 2020-05. Impact of fluidized granular flows into water: Implications for tsunamis generated by pyroclastic flows. J. Geophys. Res.: Solid Earth 125 (5).

Boussinesq, J., 1877. Essai sur la théorie des eaux courantes. In: Mémoires présentés par divers savants à l'Académie des Sciences, vol. 23, (no. 1), Impr. nationale, Google-Books-ID: QAuWqaSZqvEC.

Brackbill, J.U., Kothe, D.B., Zemach, C., 1992. A continuum method for modeling surface tension. J. Comput. Phys. 100 (2), 335–354.

Brown, S.A., Greaves, D.M., Magar, V., Conley, D.C., 2016. Evaluation of turbulence closure models under spilling and plunging breakers in the surf zone. Coast. Eng. 114, 177–193.

Bullard, G.K., Mulligan, R.P., Carreira, A., Take, W.A., 2019. Experimental analysis of tsunamis generated by the impact of landslides with high mobility. Coast. Eng. 152, 103538.

Cecioni, C., Bellotti, G., 2010. Modeling tsunamis generated by submerged landslides using depth integrated equations. Appl. Ocean Res. 32 (3), 343–350.

Chen, Q., Zhang, C., Zang, J., Ning, D., 2019. A coupled Particle-In-Cell (PIC)-Discrete Element Method (DEM) solver for fluid–solid mixture flow simulations. J. Fluids Struct. 91, 102772.

Chhabra, R.P., Richardson, J.F., 1999. Non-Newtonian Flow in the Process Industries: Fundamentals and Engineering Applications. Butterworth-Heinemann, Oxford; Boston, MA, OCLC: 182747857.

Christensen, E.D., 2006. Large eddy simulation of spilling and plunging breakers. Coast. Eng. 53 (5–6), 463–485.

Clous, L., 2018. Modelling of Waves Generated by Landslides. Discontinuous and Continuous Approaches and Focus on Energy Transfers (Ph.D. thesis). Université de Pau et des Pays de l'Adour.

Clous, L., Abadie, S., 2019. Simulation of energy transfers in waves generated by granular slides. Landslides 16 (9), 1663–1679.

Devolder, B., Rauwoens, P., Troch, P., 2017. Application of a buoyancy-modified k-omega SST turbulence model to simulate wave run-up around a monopile subjected to regular waves using OpenFOAM®. Coast. Eng. 125, 81–94.

Devolder, B., Troch, P., Rauwoens, P., 2018. Performance of a buoyancy-modified k-omega and k-omega SST turbulence model for simulating wave breaking under regular waves using OpenFOAM®. Coast. Eng. 138, 49–65.

Dumergue, L.E., Abadie, S., 2022. Numerical study of the wave impacts generated in a wet dam break. J. Fluids Struct. 114, 103716.

Fernandez-Mora, A., Ribberink, J.S., van der Zanden, J., van der Werf, J.J., Jacobsen, N.G., 2017. RANS-VOF modeling of hydrodynamics and sand transport under full-scale non-breaking and breaking waves. In: 35th International Conference on Coastal Engineering. ICCE 2016, Coastal Engineering Research Council, pp. 1–15.

Fritz, H.M., 2001. Lituya Bay case rockslide impact and wave run-up. Sci. Tsunami Hazards 19, 3.

Fritz, H.M., Hager, W.H., Minor, H.-E., 2003. Landslide generated impulse waves. Exp. Fluids 35, 505–519.

Fritz, H.M., Hager, W.H., Minor, H.-E., 2004. Near field characteristics of landslide generated impulse waves. J. Waterw. Port Coast. Ocean Eng. 130 (6), 287–302.

Greenshields, C., 2018. OpenFOAM v6 User Guide: 7.3 Transport/rheology models. OpenCFD Ltd.
Grilli, S.T., Vogelmann, S., Watts, P., 2002. Development of a 3D numerical wave tank for modeling tsunami generation by underwater landslides. Eng. Anal. Bound. Elements 26 (4), 301–313.
Grimshaw, R., 1970. The solitary wave in water of variable depth. J. Fluid Mech. 42 (3), 639–656.
Harlow, F.H., 1964. The particle-in-cell computing method for fluid dynamics. Methods Comput. Phys. 3, 319–343.
Huang, X., García, M.H., 1998. A Herschel–Bulkley model for mud flow down a slope. J. Fluid Mech. 374, 305–333.
Jánosi, I., Jan, D., Szabó, K.G., Tél, T., 2004. Turbulent drag reduction in dam-break flows. Exp. Fluids 37 (2), 219–229.
Jop, P., Forterre, Y., Pouliquen, O., 2006. A constitutive law for dense granular flows. Nature 441 (7094), 727–730.
Kim, G.-B., Cheng, W., Sunny, R.C., Horrillo, J.J., McFall, B.C., Mohammed, F., Fritz, H.M., Beget, J., Kowalik, Z., 2020. Three dimensional landslide generated tsunamis: Numerical and physical model comparisons. Landslides 17 (5), 1145–1161.
Larsen, B.E., Fuhrman, D.R., 2018. On the over-production of turbulence beneath surface waves in Reynolds-averaged Navier–Stokes models. J. Fluid Mech. 853, 419–460.
Li, Y., Larsen, B.E., Fuhrman, D.R., 2022. Reynolds stress turbulence modelling of surf zone breaking waves. J. Fluid Mech. 937, A7.
Li, Y., Raichlen, F., 2003. Energy balance model for breaking solitary wave runup. J. Waterw. Port Coast. Ocean Eng. 129 (2), 47–59.
Lin, P., Liu, P.L.-F., 1998. A numerical study of breaking waves in the surf zone. J. Fluid Mech. 359, 239–264.
Ma, G., Kirby, J.T., Hsu, T.-J., Shi, F., 2015. A two-layer granular landslide model for tsunami wave generation: Theory and computation. Ocean Model. 93, 40–55.
Mao, J., Zhao, L., Di, Y., Liu, X., Xu, W., 2020. A resolved CFD–DEM approach for the simulation of landslides and impulse waves. Comput. Methods Appl. Mech. Engrg. 359, 112750.
Mauriet, S., 2009. Simulation D'un Écoulement De Jet De Rive Par Une Méthode VOF (Ph.D. thesis). Université de Pau et des Pays de l'Adour.
Menter, F.R., 1994. Two-equation eddy-viscosity turbulence models for engineering applications. AIAA J. 32 (8), 1598–1605.
Menter, F.R., Kuntz, M., Langtry, R., et al., 2003. Ten years of industrial experience with the SST turbulence model. Turbulence Heat Mass Transf. 4 (1), 625–632.
Mohammed, F., Fritz, H.M., 2012. Physical modeling of tsunamis generated by three-dimensional deformable granular landslides. J. Geophys. Res.: Oceans 117 (C11).
Moukalled, F., Mangani, L., Darwish, M., 2016. The finite volume method in computational fluid dynamics: An advanced introduction with OpenFOAM® and Matlab. In: Fluid Mechanics and Its Applications, vol. 113, Springer International Publishing, Cham.
open source CFD toolbox, T., 2024. OpenFOAM: User Guide: Overset.
Openfoam-code, 2023. OpenFOAM ESI: User Guide v2112 - RNGkEpsilon.C source code.
Paris, A., Heinrich, P., Abadie, S., 2021. Landslide tsunamis: Comparison between depth-averaged and Navier–Stokes models. Coast. Eng. 170, 104022.
Rauter, M., Hoße, L., Mulligan, R.P., Take, W.A., Løvholt, F., 2021. Numerical simulation of impulse wave generation by idealized landslides with OpenFOAM. Coast. Eng. 165, 103815.
Rauter, M., Viroulet, S., Gylfadóttir, S.S., Fellin, W., Lø vholt, F., 2022. Granular porous landslide tsunami modelling–the 2014 Lake Askja flank collapse. Nat. Commun. 13 (1), 678.
Rodi, W., 1980. Turbulence Models and Their Application in Hydraulics - A State of the Art Review. NASA STI/Recon Technical Report A 81, p. 21395, ADS Bibcode: 1980STIA...8121395R.
Romano, A., Lara, J.L., Barajas, G., Losada, I.J., 2023. Numerical modeling of tsunamis generated by granular landslides in OpenFOAM®: A Coulomb viscoplastic rheology. Coast. Eng. 186, 104391.
Shih, T.-H., 1993. A Realizable Reynolds Stress Algebraic Equation Model, vol. 105993, National Aeronautics and Space Administration.
Shih, T.-H., Zhu, J., Lumley, J.L., 1996. Calculation of wall-bounded complex flows and free shear flows. Internat. J. Numer. Methods Fluids 23 (11), 1133–1144, Cited by: 53.
Si, P., Shi, H., Yu, X., 2018. A general numerical model for surface waves generated by granular material intruding into a water body. Coast. Eng. 142, 42–51.
Soares Frazao, S., Zech, Y., 2002. Undular bores and secondary waves -Experiments and hybrid finite-volume modelling. J. Hydraul. Res. 40 (1), 33–43.
Stoker, J.J., 1992. Water Waves: The Mathematical Theory with Applications. John Wiley & Sons, Inc., Hoboken, NJ, USA, pp. 305–308.
Tan, H., Chen, S., 2017. A hybrid DEM-SPH model for deformable landslide and its generated surge waves. Adv. Water Resour. 108, 256–276.
Tarwidi, D., Pudjaprasetya, S.R., Adytia, D., 2022. A reduced two-layer non-hydrostatic model for submarine landslide-generated tsunamis. Appl. Ocean Res. 127, 103306.
Tissier, M., Bonneton, P., Marche, F., Chazel, F., Lannes, D., 2011. Nearshore dynamics of tsunami-like undular bores using a fully nonlinear Boussinesq model. J. Coast. Res. 603–607.
Viroulet, S., Sauret, A., Kimmoun, O., 2014. Tsunami generated by a granular collapse down a rough inclined plane. Europhys. Lett. 105 (3), 34004.
Viroulet, S., Sauret, A., Kimmoun, O., Kharif, C., 2013. Granular collapse into water: toward tsunami landslides. J. Visual. 16, 189–191.
Wang, C., Wang, Y., Peng, C., Meng, X., 2017. Two-fluid smoothed particle hydrodynamics simulation of submerged granular column collapse. Mech. Res. Commun. 79, 15–23.
Weiss, R., Fritz, H.M., Wünnemann, K., 2009. Hybrid modeling of the mega-tsunami runup in Lituya Bay after half a century. Geophys. Res. Lett. 36 (9).
Wilcox, D.C., 1988. Reassessment of the scale-determining equation for advanced turbulence models. AIAA J. 26 (11), 1299–1310.
Wroniszewski, P.A., Verschaeve, J.C.G., Pedersen, G.K., 2014. Benchmarking of Navier–Stokes codes for free surface simulations by means of a solitary wave. Coast. Eng. 91, 1–17.
Xie, Z., 2013. Two-phase flow modelling of spilling and plunging breaking waves. Appl. Math. Model. 37 (6), 3698–3713.
Xu, W.-J., Yao, Z.-G., Luo, Y.-T., Dong, X.-Y., 2020. Study on landslide-induced wave disasters using a 3D coupled SPH-DEM method. Bull. Eng. Geol. Environ. 79 (1), 467–483.
Yakhot, V., Orszag, S.A., Thangam, S., Gatski, T.B., Speziale, C.G., 1992. Development of turbulence models for shear flows by a double expansion technique. Phys. Fluids A 4 (7), 1510–1520.
Yeh, H.H., Ghazali, A., Marton, I., 1989. Experimental study of bore run-up. J. Fluid Mech. 206, 563–578.
Zhao, K.-L., Qiu, L.-C., Liu, Y., 2022. Two-layer two-phase material point method simulation of granular landslides and generated tsunami waves. Phys. Fluids 34 (12).
Zhao, K.-L., Qiu, L.-c., Liu, Y., 2023. Numerical study of water wave generation by granular-liquid mixture collapse using two-phase material point method. Appl. Ocean Res. 137, 103608.
Zhou, Q., Xu, W.-J., Dong, X.-Y., 2022. SPH-dem coupling method based on GPU and its application to the landslide tsunami. Part I: method and validation. Acta Geotech. 1–19.